Article

Current Biology

Ensemble synchronization in the reassembly of *Hydra*'s nervous system

Graphical abstract

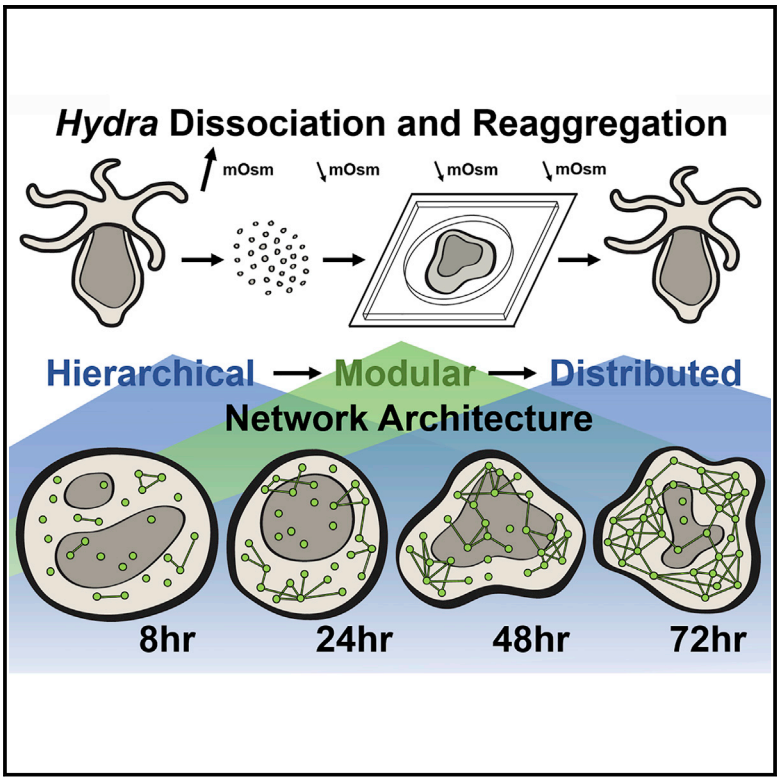

Highlights

- Reconstruction of neuronal activity during nervous system reassembly
- Uncoordinated neuronal activity becomes synchronized into neuronal ensembles
- Local ensembles merge into body-wide ensembles through hierarchical modularity
- Synchronization is due to strengthening of existing functional connections

Authors

Jonathan R. Lovas, Rafael Yuste

Correspondence

jl4548@columbia.edu

In brief

Lovas and Yuste demonstrate that, during *Hydra*'s reaggregation from dissociated cells, neurons initially are independently active and then synchronize in small neuronal ensembles. In a second step, ensembles merge across the body, generating a normal rhythm of polyp contractions.

Lovas & Yuste, 2021, Current Biology *31*, 3784–3796
September 13, 2021
https://doi.org/10.1016/j.cub.2021.06.047

CellPress

CellPress

Current Biology

Article

Ensemble synchronization in the reassembly of *Hydra*'s nervous system

Jonathan R. Lovas[1,2,3,*] and Rafael Yuste[1,2]
[1]Neurotechnology Center, Department Biological Sciences, Columbia University, New York, NY 10027, USA
[2]Marine Biological Laboratory, Woods Hole, MA 02354, USA
[3]Lead contact
*Correspondence: jl4548@columbia.edu
https://doi.org/10.1016/j.cub.2021.06.047

SUMMARY

Although much is known about how the structure of the nervous system develops, it is still unclear how its functional modularity arises. A dream experiment would be to observe the entire development of a nervous system, correlating the emergence of functional units with their associated behaviors. This is possible in the cnidarian *Hydra vulgaris*, which, after its complete dissociation into individual cells, can reassemble itself back together into a normal animal. We used calcium imaging to monitor the complete neuronal activity of dissociated *Hydra* as they reaggregated over several days. Initially uncoordinated neuronal activity became synchronized into coactive neuronal ensembles. These local modules then synchronized with others, building larger functional ensembles that eventually extended throughout the entire reaggregate, generating neuronal rhythms similar to those of intact animals. Global synchronization was not due to neurite outgrowth but to strengthening of functional connections between ensembles. We conclude that *Hydra*'s nervous system achieves its functional reassembly through the hierarchical modularity of neuronal ensembles.

INTRODUCTION

Modularity plays an essential role in evolution, as the compartmentalization of components of a system allows their independent optimization, minimizing potentially deleterious system-wide effects.[1] Modularity plays a key role in the nervous system as well, allowing the compartmentalization of specific structural and functional units.[2] In turn, modularity may be decomposed further, from modules to submodules, establishing a scaling hierarchy hypothesized to confer fast adaptation to changing environmental conditions through stable intermediates, which drastically curtails the time required for the evolution of complex forms.[3] Thus, observing the development of the hierarchical modularity of the nervous system and correlating it with the emergence of specific behaviors can help reveal the functional design logic of nervous systems.

To explore principles that guide the functional development of the nervous system, it would be ideal to study the process in its entirety. As an alternative to the complexity of commonly used model organisms, one can use *Hydra vulgaris*, a small transparent Cnidarian that is an extant representative of one of the earliest and arguably simplest nervous systems in evolution.[4,5] *Hydra*'s nervous system has an apparently simple structure distributed through the animal's ectoderm and endoderm, without any cephalization or ganglia. Furthermore, *Hydra* possesses unusual regenerative abilities and can reassemble itself after complete dissociation of animals into individual cells, a process termed "reaggregation."[6] Importantly, this process is based on the transformation of existing body tissues—morphallaxis—removing the confound of continuous cell division in standard neurodevelopment or epimorphosis-based regeneration.[7] Together with *Hydra*'s optical transparency, this remarkable regenerative ability provides a unique opportunity to observe the complete *de novo* functional development of a nervous system. Our goal was to document the activity of neurons as they assemble into circuits throughout the process, providing insight into the emergence of modularity and its role in shaping network topology and dynamics.

Here, we imaged the activity of neurons in reaggregating *Hydra* preparations as normal neuronal rhythms recover during the first 72 h post-dissociation. We report that *Hydra*'s nervous system synchronizes during its reassembly through a two-step process in which the initially uncoordinated activity of small groups of neurons clusters into coactive ensembles, concomitant with pronounced local increases in connectivity and neurite outgrowth, followed by the synchronization of these local ensembles across the entire body of the animal and re-establishment of behavioral rhythms at 72 h.

RESULTS

Circuit synchronization re-established 72 h after dissociation

To study the functional development of *Hydra*'s nerve nets as they regenerate, we mechanically dissociated tissue into individual cells by triturating GCaMP6s neuronal transgenic animals with a glass Pasteur pipette after incubation in relatively high-osmolarity media (Figure 1), similarly to established protocols (STAR Methods).[6] Regenerating aggregates were imaged for 30-min periods on an epifluorescence microscope at 8, 24, 48,

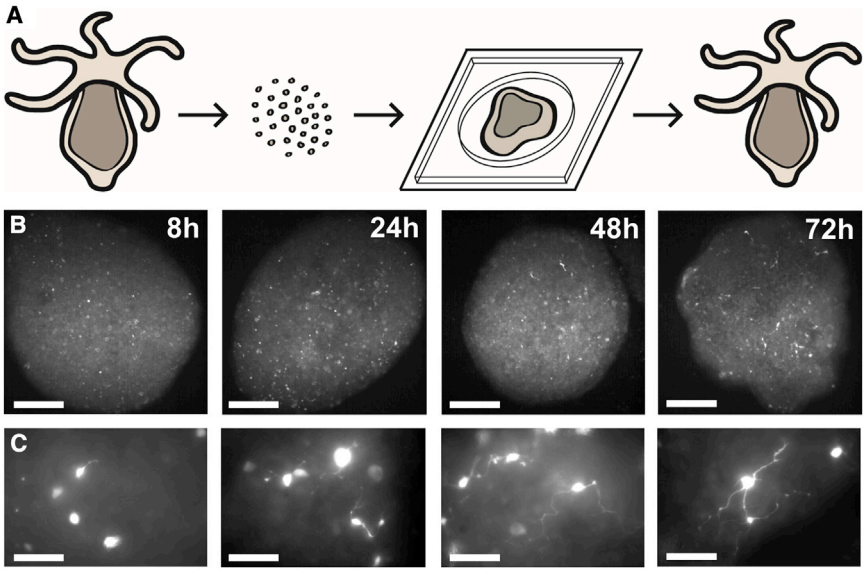

Figure 1. *Hydra* dissociation and reaggregation

(A) Experiment workflow. Hydra were mechanically dissociated into individual cells after a 2-h incubation in higher osmolarity dissociation media. At various intervals throughout the process, regenerating cellular aggregates were mounted and imaged to monitor changes in the functional architecture of developing neural circuits. After enough time, aggregates re-established body axes, grew tentacles, and were indistinguishable from undisturbed animals.

(B) Representative images of neuronal GCaMP fluorescence in aggregates at experimental time points. Scale bar, 200 μm.

(C) Representative images of neuronal GFP in reaggregates diluted 1:25 with wild-type animals to isolate neurite outgrowth for analysis at different time points. Scale bar, 50 μm.

See also Figure S1 and Data S1G.

and 72 h post-dissociation in mounted coverslip preparations,[4,8] while intact animals were imaged on a dissection microscope, as previously described.[4] Animals in all experiments eventually regenerated to yield normal hydranths.

We first investigated how long after dissociation it takes for normal contractile rhythms to reappear. Visual inspection of the movies showed that, after 72 h, aggregates already displayed the two major forms of synchronized neuronal activity found in mature animals: rhythmic potentials (RPs) and contraction bursts (CBs) (Figure 2A; Video S1; n = 5/6 experiments; p = 1; Fisher's exact test). To analyze circuit activity, we measured the fluorescence intensity changes of all neurons and manually annotated RPs and CBs.[4,9,10] We observed a significantly higher frequency of CBs in 72-h aggregates versus intact animals (Figure 2B; Data S1B; n = 5 experiments), complemented by a decrease in the number of pulses per CB (Figure 2B; Data S1B). At the same time, there were no significant differences in total percentage of time spent in burst (Figure 2B; Data S1B) or in CBs pulse frequency (Figure 2B; Data S1B). Given the increased CB frequency at 72 h and the independence of opposing RP and CB circuit activity, we observed decreased RP circuit activity at 72 h (Figure 2B; Data S1B). We concluded that aggregates recuperated animal-wide neuronal activity patterns by 72 h and concentrated the rest of the study on earlier changes in circuit activity.

Hydra neurites elongate during the first 48 h of reaggregation

To understand the structural underpinnings of reaggregation, we next explored neurite outgrowth. To visualize individual neural processes, we mixed neuronal GFP animals into a reaggregation of wild-type (AEP) *Hydra*. Albeit with large variability likely due to intrinsic differences in neuronal subtypes,[4,11] by 48 h, *Hydra*'s neural processes were similar to those observed at 72 h in the length of neurites (Figures 1 and S1A; Data S1G) and number of branches per neurite (Data S1G). We concluded that a majority of neurite outgrowth occurred during the first 48 h of reaggregation, indicating that neuronal outgrowth alone cannot explain the changes in functional connectivity leading to the re-establishment of animal-wide activity from 48 to 72 h.

Changes in neuronal activity during reaggregation

To better quantify synchronization during reaggregation, we imaged calcium activity of individual neurons in 30-min time lapses collected at 0, 8, 24, 48, and 72 h. Images were preprocessed, and the positions of GCaMP6s-labeled neurons visible on the aggregate were tracked with ICY (STAR Methods).[9,10] After thresholding and manual curation of the dataset to fix errors in tracking,[4,12] we found a gradual decline in the number of active neurons per aggregate (Figure S1B; Data S1G; STAR Methods), consistent with the expected loss of unintegrated cells.[13,14] Spike rasters were then generated for each experiment (STAR Methods; Figure S1C; Video S2). We observed a gradual increase in neuron firing rate from 8 h to 48 h, with a drop at 72 h to levels similar to dissociated cells (Figure S2A; Data S1H). Interspike intervals (ISIs) showed a reverse pattern (Figure S2B; Data S1H). We observed that the ISI variance-to-mean ratio (VMR) of neurons across all time points underwent a pivotal intersection around 100 s—approximately 60% of ISI VMR values—with increasingly larger values with time until this point and smaller values beyond it (Figures S2B and S2C; Data S1H). At 72 h, the narrower distribution of values captured the re-establishment of *Hydra's* contraction burst circuitry, as these neurons have a larger ISI VMR in 72-h aggregates and the intact animal (Figures 2 and S2C; Data S1B and S1H). From single-cell analysis of neuronal firing, we concluded firing frequency during reaggregation displays biphasic dynamics, with initial increases followed by decreases in activity, while burstiness displays a reverse dynamics, ending with a normal pattern of contraction bursts.

Increases in functional connectivity during reaggregation

To detail the synchronization in *Hydra*'s nerve net, we used graph theory, treating neurons as nodes and significant functional connections thresholded from coactivity between neurons as edges

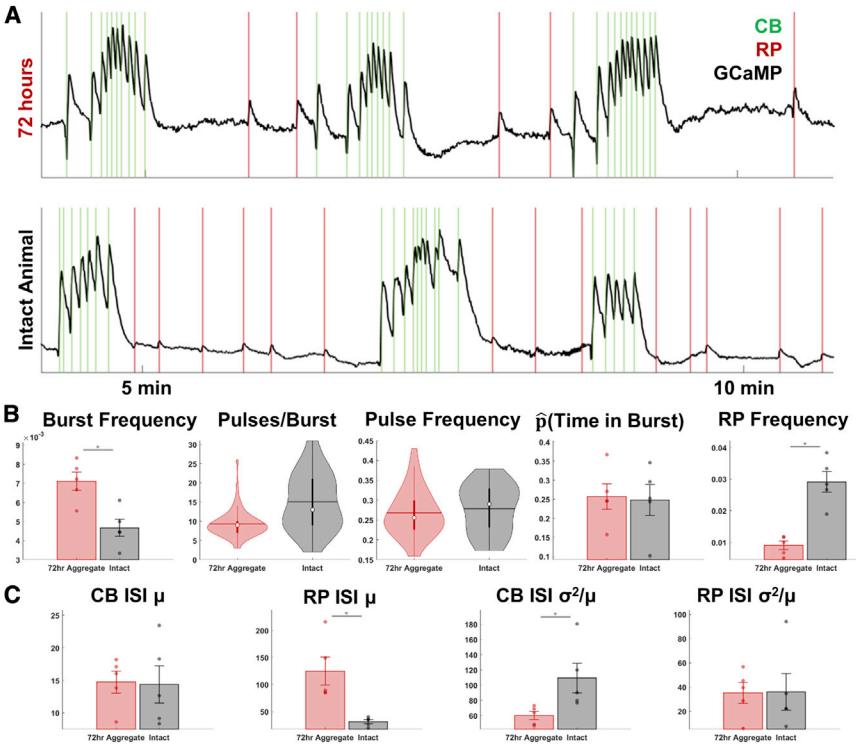

Figure 2. Animal-wide synchronization restored 72 h after dissociation

(A) At 72 h, synchronized rhythmic potentials (red) and contraction burst (green) activity are clearly discernable in manually annotated whole-animal calcium (GCaMP6s) fluorescence.

(B) 72-h aggregates show a significantly higher frequency of contraction bursts (CBs) yet fewer pulses per burst, leading to a similar percentage of time spent in CB. No significant differences in contraction pulse frequency were seen, while rhythmic potential activity (RP) was less in the 72-h aggregates compared to intact animals (n = 5 experiments).

(C) No significant differences between 72-h and intact animal CB inter-stimulus intervals (ISIs) were observed, with a higher variance-to-mean ratio (VMR) observed in intact animals. 72-h aggregates had larger RP ISIs, with similar RP ISI VMRs. Note the larger CB ISI VMRs compared to RP ISI VMRs, indicative of circuit "burstiness" (n = 5 experiments).

See also Figure S2 and Data S1B and S1H.

(n = 6; STAR Methods; Figure S3A). Consistent with the peak of neurite outgrowth at 48 h, we observed the most dramatic increase in the number and strength of significant functional connections between 24 and 48 h (Figure 3; Data S1C). The shorter distance between significant functional connections observed at 48 h could underlie differences in aggregate behavior, when compared to 72 h (Figure 3; Data S1C). These results support two phases of functional self-assembly, with pronounced local increases in connectivity and neurite outgrowth during the first 48 h, followed by the re-establishment of behavioral rhythms at 72 h.

Network restructuring during reaggregation

These observations suggested the synchronization of *Hydra*'s nerve nets began locally. In one scenario, this synchronization could arise rapidly across the entire aggregate, akin to the development of a coarse topology along morphogenic gradients before activity-dependent refinement.[15,16] In our *Hydra* data, however, this time course was not as steep as other models (Figure 3).[17,18] In the absence of extensive structural patterning, we wondered whether an alternate mechanism relating to the emergence of hierarchical modularity might be in play, given that modularity confers evolvability and robustness, allowing nature to act independently on duplicates of a single module.[1]

To explore this, several standard graph theoretic metrics of network structure and function were applied to binarized network models, thresholded at the α = 0.005 significance level, with controls for network size and connection density (Figures 4A, 4B, 4D, and 4E, dashed lines; Data S1D) and the removal of unintegrated neurons from the developing network (STAR Methods; Figure S3B; Data S1I).[19] We analyzed degree distributions, clustering coefficients, and betweenness centrality of the binarized networks, as these metrics can be used to infer hierarchical modularity. We found an expected increase in mean degree (k) with aggregate age (Figure 4A; Data S1D). The heavy tail in the degree distributions at earlier time points, before the saturating effect of network size, was reminiscent of "scale-free" network structures in which the ratios of values in the log-log linear distribution are the same regardless of the scale of observation (Figure S3C; Data S1I). Truncating our distributions to nodes with a degree less than one-third of the size of the network yielded better fits at 48 and 72 h (Figure S3B; Data S1I).

Although *Hydra*'s developing networks in our experiments were not large enough to confirm the presence of scale-free network structures, we were intrigued by the heavy-tailed trend in the data, because scale-free networks are moderately hierarchical and can reflect dynamics on the verge of a phase transition.[20–22]

Hydra's nerve net becomes increasingly distributed during reaggregation

We tested for the existence of hierarchical modularity by analyzing additional network properties. We observed an increase in the clustering coefficients of nodes—any two significant functional connections to a neuron were increasingly likely to also be significantly coactive with each other—both in terms of the number of nodes with any clustering (Figures 4B and 4E; Data S1D), as well as the strength of this coefficient (Figure 4B; Data S1D). In addition, a key feature of hierarchical modularity in networks is the presence of nodes with high "betweenness centrality," which form interconnections between densely intraconnected modules to route the graph's shortest paths.[23] Indeed, measures to calculate the betweenness centrality of large networks exploit hierarchical structure for efficiency.[24] While no significant differences in node betweenness centrality emerged between 8 and 24 h, at later stages, we detected a

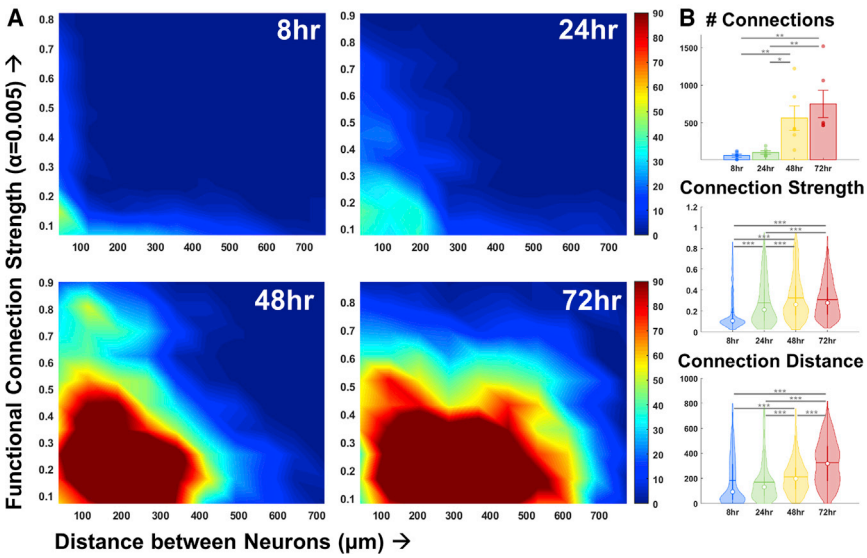

Figure 3. Synchronization increases during reaggregation

(A) Heatmaps of pairwise connection strengths (y axis) between neurons as a function of distance (x axis) for significantly connected neurons at the α = 0.005 threshold, determined by circularly permuting binary neuron spiking rasters at random initiations 1,000 times. Note the local increases in connection strength before synchronization across the animal at 72 h.

(B) We detect a significant increase in the number of significant connections at the α = 0.005 threshold moving from 24 to 48 h. Within these significant connections, connection strength gradually increases until a plateau at 48 h. A significant increase in the distance of these connections from 48 to 72 h highlights the local optimization of circuitry before synchronization across the entire animal.

See also Figure S3 and Data S1C and S1I.

gradual redistribution of *Hydra*'s network structure, both in terms of the number of nodes with any betweenness centrality (Figures 4C and 4F; Data S1D), as well as the strength of this coefficient (Figure 4D; Data S1D). Edge betweenness values showed a similar trend (Figures 4D and 4F; Data S1D). Thus, the redistribution of *Hydra*'s network structure supported the hypothesis that the emergence of synchronization can be explained by increases in the strength of functional connections between ensembles.

Network hierarchical depth diminishes during reaggregation

We next considered these node metrics as a function of node degree (Figures 4E and 4F). Hierarchical modularity can be inferred from a decrease in the clustering coefficient (C) of nodes with increasing degree (k), as low-C and high-k nodes may link disparate, otherwise weakly connected modules of nodes.[22] Indeed, we found a decline in clustering coefficients of nodes as their degree centrality increased from 8 to 48 h (Figure 4E; Data S1D). The negative fit slopes along the log-log plot indicated a hierarchically modular network structure at 8 and 24 h, and the gradual decrease of the slope magnitude with time indicated a loss of hierarchical depth, consistent with our observations of the redistribution of betweenness centrality values. While the trend persisted to 48 and 72 h, this decline suggested the disparate modules these nodes linked increasingly shared additional edges with each other, a potential "module overlap" supported by the dramatic increase in the number of nodes with values above what would be expected in random graphs of the same density, as visualized by the gray cloud of values reflecting p = 0.05 C(k) (STAR Methods; Figure 4E; Data S1D). Similarly, when examining node betweenness centrality (B) as a function of k, at 24 h, we noticed nodes with *smaller* B(k) values than would be expected at random (Figure 4F; Data S1D). This suggested an early increase in modularity from 8 to 24 h, as nodes deep in densely intraconnected modules have lower betweenness centrality values relative to their degree. This trend grows increasingly prevalent at 48 and 72 h, accompanied by increases in the number of nodes with *larger* B(k) values versus the same isopycnic random networks (Figure 4F; Data S1D). At 48 h, these relatively high B(k) nodes likely correspond to links between modules, and the increase in the number of nodes with lower B(k) values than expected suggests the presence of modules linked by these high B(k) nodes, a feature that extends to data at 72 h.

Taken together with the increases in the strength of functional connections (Figure 3), these results suggested a mechanism of synchronization where a small number of significantly connected nodes routed a more significant portion of network traffic at earlier time points at the top of a hierarchy, which grew increasingly distributed as clustering increased and these smaller groups of significantly connected nodes began to overlap in activity. Our results suggested a role for modularity in this process, so we then explored this with a more formal definition of the concept.

Emergence of modularity accompanies loss of hierarchical depth

The modularity of biological networks generally increases with complexity in metazoans,[25] and modules are often hierarchically structured.[26,27] Given the recent discovery of pattern completion neurons and their implications for the hierarchical structure of neural circuits in mammalian cortex,[28] we explored whether the hierarchical structure of *Hydra*'s nervous system was related to modularity. To do so, we used the Louvain algorithm to partition weighted network models of multineuronal activity into ensembles, i.e., modules, or "communities" (STAR Methods; Figure S4).[29–31] We observed both increases in community strength and changes in community structure as reaggregation progressed (Figure 5). The average coactivity of each node with every other node in its community increased with time (Figure 5A; Data S1E). A similar although less extreme trend was observed comparing the ratio of intra- to intercommunity connection strengths (Figure 5B; Data S1E). Taken together, these observations indicated that increases in intracommunity strength drove this effect, given that the majority of values of the intra- or intercommunity strength were greater than unity.

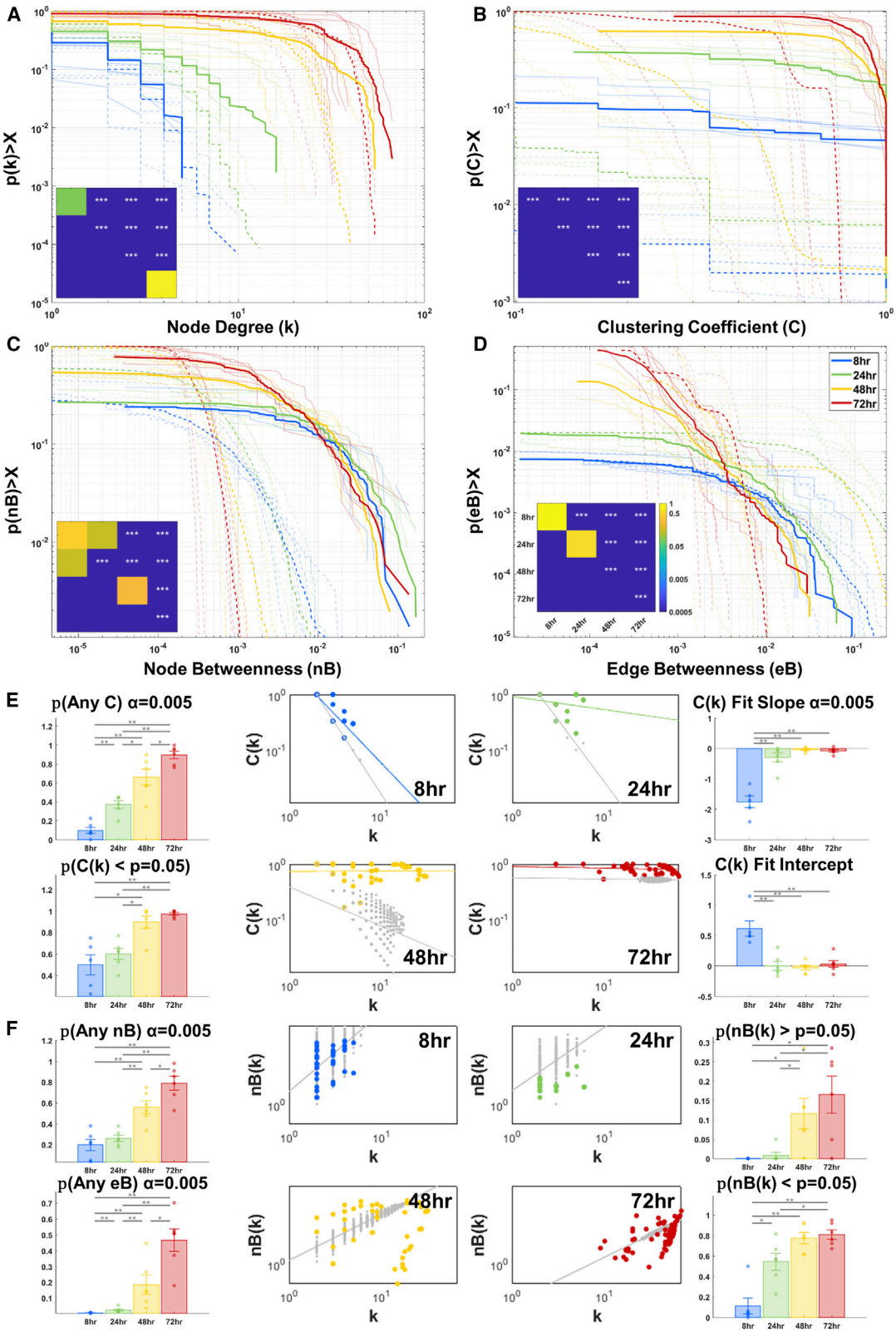

(legend on next page)

Consistent with our observations of strong edge weights at low distances at 48 h (Figure 3), intracommunity distances were significantly smaller at this time point (Figure 5C; Data S1E). Correspondingly, ratio of intra- to intermodule physical overlap of nodes peaked at 48 h, determined using a radius of the average neurite length at 48 h as potential physical connectivity (Figure S5; Data S1K). This intermediate state of relatively high functional and spatial modularity prompted us to explore how it evolved during the process.

Modularity arises from synchronization of smaller ensembles

We hypothesized that our observed modules might be built from the interaction of small ensembles that form early during reaggregation. To dissect this potential containment hierarchy, we used the Louvain algorithm again to partition our initial detected modules into sub-communities (Figures 5G and 5H), inspired by previously described methods.[32] While the maximum modularity of our initial partitions was similar at 24 and 48 h (Figure 5H; Data S1E), the modularity of the entire subdivided network decreased more at 48 h, compared to 24 h (Figure 5H; Data S1E). Correspondingly, the modularity of partitions of initial modules was highest at 24 h (Figure 5H; Data S1E), and more subdivisions of the modules were made (Figure 5H; Data S1E). At every time point, the distance between members of the sub-communities was smaller than distances between neurons of their parent communities (Figures 5G and 5H; Data S1E). Furthermore, the increase in the ratio of intra- to intermodule spatial overlap, moving from our initial to sub-partitions, was largest at 24 h (Figure S5; Data S1K). Taken together, this indicated the emergence of modularity through the interaction of smaller ensembles of neurons and provided initial evidence to distinguish the similar maximum modularity values of the initial partitions at 24 and 48 h.

We obtained further insight into the hierarchical structure of detected Louvain communities by examining community metrics at different resolutions, using a sweep of the modularity resolution parameter gamma from 0.6 to 3 in increments of 0.01 (STAR Methods; Data S1J).[32–36] We found an increase in the stability of partitions with increasing aggregate age (Figure S4B), as indicated by the dramatic increase in the number of plateaus from 8 to 24 h (Data S1J) and the significant increase in plateau length from 24 to 48 h, consistent with the maximum modularity observed at 24 and 48 h (Data S1J).[37] While aggregates at 24 and 48 h showed the highest modularity at the peak near unity, values at 24 h declined less rapidly as gamma increased (Figures S4B and S4C; Data S1J). This accompanied a larger increase in the number of communities at 24 h compared to later time points (Data S1J), indicating the network was more efficiently partitioned into smaller communities. This stability at 24 h represents another form of containment hierarchy, as smaller communities are necessarily derived from the larger communities at the start of the sweep.

Phase transition through a critical regime of activity

A striking feature of the process of vertebrate neural development is waves of activity that spread throughout locations of the nervous system.[38,39] In some cases, these "neuronal avalanches" follow a power-law distribution indicative of a scale-free critical regime of activity.[40,41] The presence of power-law scaling supports the hypothesis that the cortex operates at a state of self-organized criticality, on the verge of a phase transition.[40–42] Consistent with this, waves of activity were present in aggregates at all time points when examining the propagation of coactivity between neurons (STAR Methods; Figures 6 and S6; Video S3). Features of these waves, such as duration or size, showed heavy-tailed trends, more pronounced at earlier time points. At 8 h, *Hydra*'s dynamics appeared close to a critical regime of activity and became increasingly supercritical thereafter, indicative of what may be considered a phase transition (Figure 6A; Data S1F).[43] The lack of clear differences in the duration of avalanches across time points suggested that larger avalanches may be due to the coincident activity of modules, the spreading of activity between modules, and increased "burstiness" of modules re-recruited to spreading waves (Figure 6B; Data S1F). Indeed, comparison of the duration of avalanches as a function of their size supports this (Figures 6C and 6D). The burstiness of synchronized CB circuitry at 72 h and the drop in the distribution of avalanche durations compared to earlier time points aligns well with modeling of contractions of the bell of the jellyfish *Aurelia aurita*, where the refractory period of neurons limits the spread of waves of activity to a single contraction.[44]

The increased dynamic range of hierarchical modular network architectures supports sustained critical activity more effectively

Figure 4. Hierarchy decreases during reaggregation

(A) Using binary networks thresholded at $\alpha = 0.005$, we see a gradual increase in the distribution of node degree with time in the log/log descending cumulative distribution plot. Dotted lines represent the distribution of values obtained with 20 network randomizations; diagonals on the "significance matrices" (bottom left of plots) represent comparison of experiment values to this random distribution.

(B) Increases in the distribution of node clustering coefficient follow a similar trend, indicating that two nodes connected to any given node are increasingly likely to be connected themselves.

(C and D) Node betweenness (C) and edge betweenness (D) reveal the gradual shift toward a distributed network structure at 72 h, when normalized to the total number of edges in the network.

(E) An increasing number of nodes show any clustering with time (top left). Node degree and clustering coefficient, taken together, allow analysis of any hierarchical modularity as conceptualized by Ravasz and Barabasi, as depicted in a representative experiment (middle). A significant increase in the number of nodes above C(k) values that would be expected compared to 20 network randomizations (plotted in gray for a representative experiment, middle) is observed from 24 to 48 h (lower left). The decreasing slope of the fits at 8 and 24 h is indicative of hierarchical modularity, while this trend is lost at 48 and 72 h as *Hydra*'s nervous system synchronizes (right).

(F) In the case of both edges and nodes, significantly more elements are participating in the routing of information across the network with aggregate age, as opposed to the handful of nodes at 8 and 24 h handling most of the shortest paths within the network (left). Node betweenness centrality plotted as a function of node degree, with values for 20 network randomizations plotted in gray (middle), is shown. From 24 to 48 h, we observe a significant increase in the number of nodes above the $p = 0.05$ gray probability cloud and a significant increase from 8 h to 24 h in the number of nodes with values below the probability cloud (right). See also Figure S3 and Data S1D and S1I.

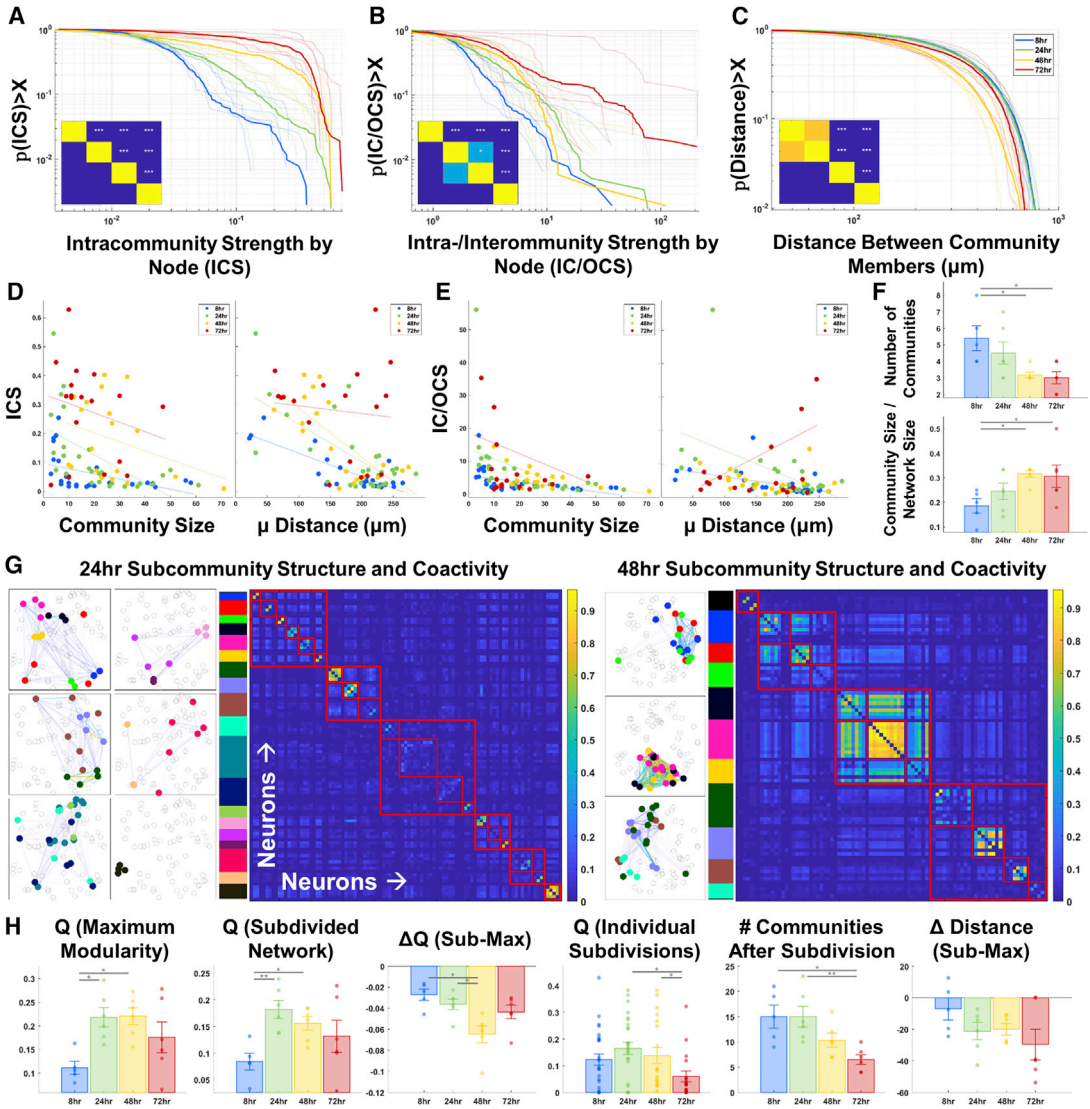

Figure 5. Decrease in modularity during reaggregation

Taking Louvain consensus communities of the partition with the maximum modularity of all plateaus across a modularity resolution sweep for each experiment, details of community structure across the course of reaggregation are revealed.

(A) During reaggregation, we see a drastic increase in the distribution of intracommunity strengths by node with aggregate age.

(B) This trend is also present for the ratio of intra- to intercommunity strength, indicating that, while the strength of connections within communities is increasing, the strength of intercommunity connections is increasing as well. Importantly, most values of the ratio of intra- to intercommunity strength are greater than 1, indicating that intracommunity strength is increasing at a greater rate.

(C) The local synchronization of circuitry before the global synchronization observed at 48 h is captured by the reduced distance between nodes of the partition with maximum modularity at 48 h.

(D) Intracommunity strength as a function of community size (left) and mean distance between members (right) for all detected communities.

(E) Intra- and intercommunity strength ratio as a function of community size (left) and mean distance between members (right) for all detected communities.

(F) From 8 h to later time points, we observe a decline in the number of detected communities (top) and an increase in the community size relative to network size (bottom).

(G) Adjacency matrices of neuron connection strength at 24 and 48 h organized by Louvain partitions of the network (larger red squares) and sub-partitions of these initial detections (smaller red squares). Spatial arrangement of the partition of the entire network indicated by panels to the left of adjacency matrices, color coded by membership in community sub-partitions (between the spatial arrangement and adjacency matrices). Note the smaller distance between members of strongly connected sub-partitions (edge weight scale bar to the left of adjacency matrices).

(H) From left to right: modularity of partitions of the entire network is highest and similar at 24 and 48 h. The modularity of the entire subdivided network is highest at 24 h. The largest drop in modularity for sub-partitioning occurs at 48 h. The modularity of individual subdivisions is highest at 24 h. There is a decline in the number of communities with sub-partitioning after 24 h. At all time points, the average distance between community members decreases with sub-partitioning of the network.

See also Figure S4 and Data S1E and S1J.

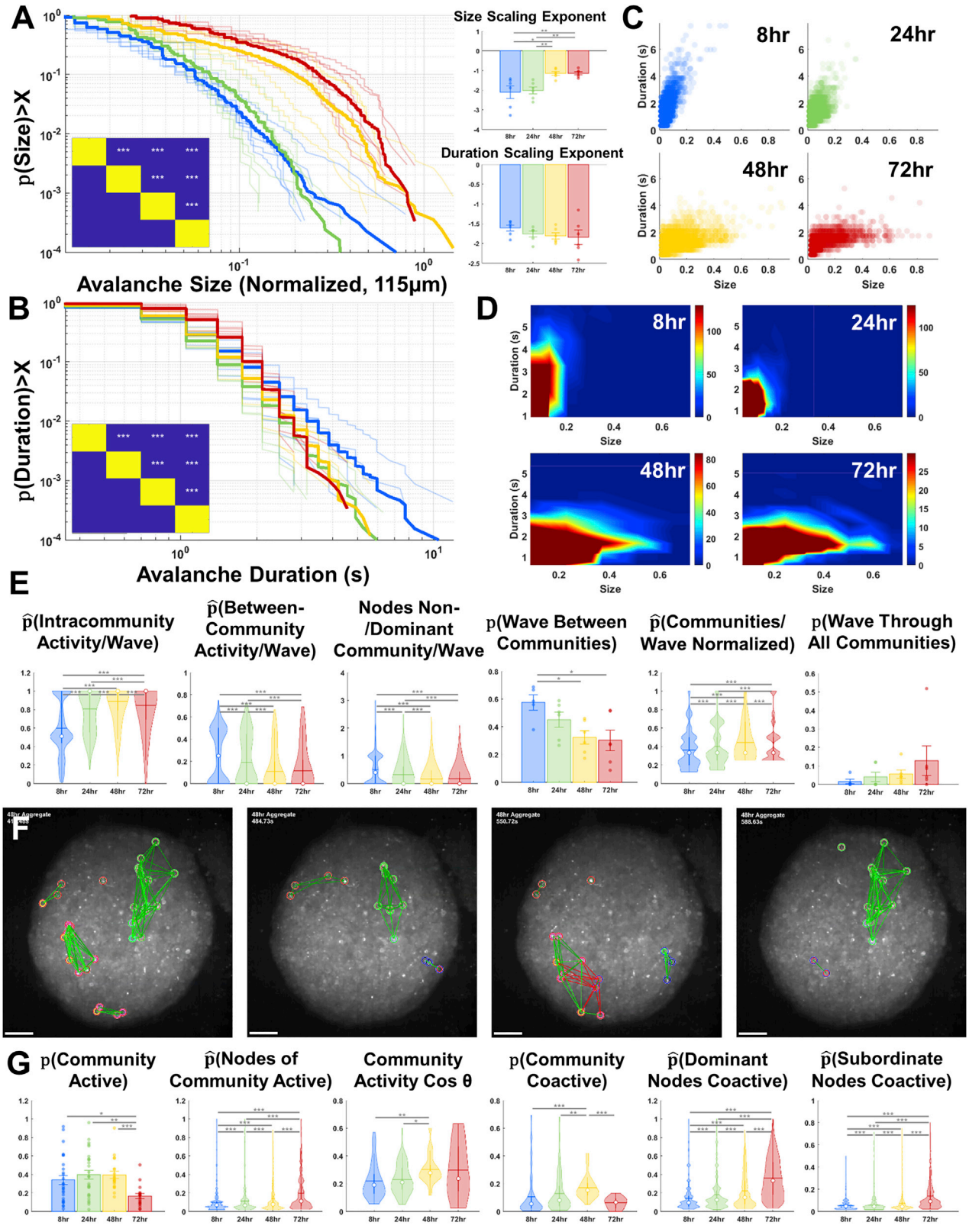

(legend on next page)

than distributed architectures.[45] To explore this, we examined avalanches within our initial Louvain communities (Figures 6E–6G; Video S4). We were increasingly likely to see intracommunity coactivity as part of a wave to 48 h (Figure 6E; Data S1F) and less likely to see intercommunity activity (Figure 6E; Data S1F). In addition, considering the "dominant module" as that with the most nodes comprising the wave, we detected a decreasing percentage of nodes from non-dominant communities to 48 h and, similarly, a smaller probability of observing waves traveling between communities (Figure 6E; Data S1F).

Synchronization of modules via shared neurons

To further distinguish the similar maximum modularity values at 24 and 48 h (Figure 5G), we examined interactions between initial Louvain modules by generating raster plots of the combined activity of all neurons in a module. Consistent with the synchronization observed by 72 h (Figure 2) and the gradually increasing firing rate of neurons up to 48 h (Figure S3), we found a decrease in the probability of finding any node from a particular community active at 72 h (Figure 6G; Data S1F) and a gradual increase in the proportion of nodes of a community active during any activity at 72 h (Figure 6G; Data S1F). In contrast to the reduced spread of waves of activity between *any* modules at 48 h (Figure 6E), we found the probability of observing coincident activity of *two* compared communities rises at 48 h (Figure 6G; Data S1F), a reflection of the increased firing rate of neurons at this time point (Figure S2A), the radius of detection wave activity (STAR Methods), and community size, in combination with the reduced distance between module neurons at 48 h (Figure 5C). The cosine similarity of the activity of each community with each other was largest at 48 h, indicating that parts of distinct modules increasingly fired together (Figure 6G; Data S1F). To confirm this, we divided any coactivity between communities into a dominant and subordinate community based on the number of nodes each contributed. We observed gradual increases in the proportion of nodes in any coactivity in both the dominant and, importantly, the subordinate community, across our experiment time points (Figure 6G; Data S1F).

These results helped distinguish observations of similar maximum modularity at 24 and 48 h, putting the stability of modularity at 24 h into context. Our observations of *local* increases in strength at 48 h to levels almost that of 72 h suggests higher modularity than at 24 h (Figure 2). However, at 48 h, any coactivity of two modules on average contains 26% of the nodes of the more active, as well as 8% of the nodes of the less active module, which necessarily increases the out-of-module connection strength with our observed increases in within-module strength (Figures 5 and 6). This suggests a route to synchronization where smaller groups of coactive cells increasingly share occasional coactivity with multiple other groups. More regular coactivity between groups defines the detected modularity, while coactivity outside these defined communities raises the valley between detected modules and detracts from our observed modularity values (Figure 6G).

DISCUSSION

Local self-assembly of the nervous system during *Hydra*'s reaggregation

In this study, we leveraged the ability to image the activity of the entire nervous system in *Hydra*[4] to study the mechanism of neural circuit assembly during the *de novo* self-assembly of its nervous system from dissociated cells (Figure 7). Neural circuit synchronization was largely recovered across the entire animal after 72 h (Figure 2). Examining earlier time points, neurite outgrowth slowed at 48 h (Figures 1 and S2), and the strength of most functional connections was as strong as at 72 h (Figure 3). Intriguingly, the distance between functional connections was significantly shorter at 48 h, suggesting a local optimization of circuitry before synchronization across the entire animal. This developmental trajectory shares key similarities with increasingly complex systems. For example, in the zebrafish spinal cord, although cellular migration plays an essential role before the onset of neural activity, a rapid synchronization is observed from 18 to 22 hpf. Reminiscent of the changes that occur in *Hydra*, small "ensembles" form at distinct points before recruiting additional neurons and eventually synchronizing across segments.[17,18]

Figure 6. Avalanches recruit module sub-circuits during synchronization

(A) During the course of reaggregation, distributions of the sizes of neuronal avalanches (left) and critical exponents (top right) suggest a phase transition in activity of the regenerating nervous system as the system becomes increasingly supercritical. Note the clear shift in sizes along the x axis is due to normalization to the number of nodes in the network and that waves of activity were generated using a 115-μm radius of coactivity (twice the average neurite length at 48 h; Figure S1).

(B) Distributions of avalanche duration are not as distinct.

(C) Dot plot of avalanche duration as a function of size. Note the distinct cluster at 48 h.

(D) Heatmaps providing more resolution of densely clustered points near the origin of the duration (size) plots.

(E) Superimposition of neuronal avalanches on detected Louvain communities at maximum modularity. From left to right: coactivity of neurons within the avalanche wave radius of 115 μm is increasingly likely to be in the same community to 48 h. Coactivity between communities declines to 48 h. Fewer nodes from a non-dominant community are likely to be recruited to a wave to 48 h. Waves are increasingly less likely to spread between communities to 48 h. A trend toward more communities per wave normalized to the total number of communities with time is present. A trend toward an increasing number of waves traveling through all communities is present.

(F) Demonstration of circuit and sub-circuit activity at 48 h. Outer circle colors represent larger Louvain network partitions; smaller circle colors represent sub-partitions.

(G) Rasters of the summed activity of all neurons in each of the detected communities at maximum modularity. From left to right: consistent with firing rate (Figure S3), communities are less likely to be active at 72 h. When communities are active, an increasing proportion of nodes of a community are likely to be active, consistent with increased recruitment to neurons to developing circuitry. The cosine similarity of these community rasters increases at 48 h, indicating community activity is more similar than earlier time points. The probability of finding coactivity between communities increases to 48 h. Consistent with the increased cosine similarity of community activity at 48 h, when community coactivity is divided into a dominant and subordinate community based on the number of neurons active at each point of coactivity, the proportion of nodes of the dominant community as well as the subordinate community increases with aggregate age.

See also Figure S6 and Data S1F and S1L.

Network activity becomes distributed during reaggregation

Using network modeling, we observed the early formation of a containment hierarchy from 8 to 24 h, as measured by the relationship of node clustering coefficients to node degree (Figures 4A, 4B, and 4E). This aligned well with the observed heavy-tailed degree distributions at earlier time points, a characteristic of log-log linear distributions of putative scale-free network structures (Figures 4A and S3). In addition, measures of betweenness centrality revealed a shift to a distributed network structure over the course of reaggregation (Figures 4C, 4D, and 4F). This transition from a hierarchical structure to a distributed structure can be interpreted in light of the fact that distributed systems are generally more scalable and resilient than other architectures. Indeed, it might be argued that *Hydra*'s distributed nervous system facilitates this extreme regeneration in the first place, allowing immature ensembles to form and resume their function less discriminately than more highly patterned systems. Our analysis suggests that the C(k) containment hierarchy mediates interconnections between these immature ensembles via hub nodes. The loss of this rigid hierarchical structure is inherent in the eventual fusion of these ensembles as regeneration progresses.

Self-assembly during reaggregation is mediated by hierarchical modularity

To understand hierarchical modularity further, we partitioned the network into modules and submodules and explored the dynamics of their activity. With time, our detected modules showed increases in intracommunity strength and the ratio of intra- to intercommunity strength, driven by increased intracommunity strength (Figures 5A and 5B), and nodes of detected modules at 48 h were generally less distant (Figure 5C). By partitioning the network into submodules, we observed more stability of modularity and a larger increase in the number of communities at 24 h, indicating more smaller, densely connected ensembles (Figures 5G, 5H, and S5).

Hierarchical modularity plays a role in the evolvability of complex systems by generating stable intermediates during evolutionary processes.[3] Several studies indicate that modularity arises from temporally and modularly varying sub-goals—where each new sub-goal shares problems with the previous sub-goal[46,47]—and that the emergence of hierarchical modularity during network development is a result of placing selective pressure to minimize connection costs.[48,49] *Hydra*'s need to synchronize the nervous system likely takes utmost priority in regeneration and arguably provides motivation to break the process into sub-goals and minimize connection costs. Amid significant cell death due to the traumatic process of dissociation,[13,14] *Hydra* must establish body axes in the appropriate orientation via morphallaxis,[50] re-establish neuromuscular transmission to allow active osmoregulation,[51] and synchronize the nervous system so animal-wide behavior can be coordinated. Given that each of these related sub-goals can be initiated at independent sites in the aggregate and share a need for intact circuitry, it can be argued that the modularity we see reflects effort to address these sub-goals with a common need for local optimization of circuitry as opposed to extensive neurite outgrowth. The synchronization of wounded neurons, particularly at longer distances, clearly poses a risk to aggregate integrity if these cells are eventually lost. From this, our observed modularity may arise from a process of sorting and viability assessment locally before synchronization across the animal, as opposed to the rapid coordination observed in grafting experiments, where halves of grafted *Hydra* synchronize within hours.[52] The necessity of minimizing connection costs during reaggregation stands in contrast to the redundancy of the circuitry of the intact animal, whose behavior is constant over a wide range of sizes of animal,[53] with variable numbers of neurons depending on the nutritional status of the animal.[54] Thus, the loss of an intermediate state of hierarchical modularity in *Hydra* fits well into the strategies used by the animal to negotiate the new goals that arise with changing complexity.

Self-organized criticality with scale-free properties in *Hydra*'s reaggregating networks

We noticed neuronal avalanches with statistics reflective of a phase transition through a critical regime of activity (Figures 6A–6D). While the coactivity of neurons comprising smaller waves at 24 h traveled through communities more readily, when one community was active at 48 h, it generally recruited more nodes of additional communities, as another distinction of the increased modularity values observed at 24 and 48 h (Figures 6E–6G). As modules gradually became more defined, they eventually became coactive with each other as synchronization spread across the entire animal (Figure 6). This fusion of modules late in the process likely contributed to the decline in modularity we observe at 72 h, an extension of the sub-circuit coactivity across modules observed at 48 h (Figure 6H). While a majority of circuit activity was synchronous, defined sub-circuits occasionally fired in isolation (analogous to CB and CB' sub-circuitry in the intact animal), creating detectable partitions in the network that diminished modularity at this time point.[4,9,11,12]

Hierarchical modular networks sustain critical activity across a wider range of parameter spaces (e.g., synapse strengths) than sparse networks without hierarchical modularity.[55,56] Consistent with our observations (Figure 6), theory suggests that modules may act as subsystems, providing weak input to others to propagate neuronal avalanches in a delicate balance compromised by too much or too little modularity.[55–57] The present study provides *in vivo* support of this theory (Figure 7), given that the loss of hierarchical modularity is coincident with the shift in avalanche dynamics into what might be considered an increasingly supercritical regime of activity. In addition, this supercritical burstiness at later time points aligns well with observations of deflections of the avalanche size probability distribution due to stimulus-elicited activity in zebrafish, where self-generated behavior results in faster, larger, and longer avalanches due to the recruitment of intact circuitry.[58]

Functional considerations

Our observations of diminishing hierarchy during circuit consolidation integrates well with Simon's notions of "near decomposability" in symbolic information-processing systems. The C(k) containment hierarchy suggests the existence of hub nodes mediating interconnections between proto-modules and immature ensembles formed on their way to the intermediate state of maximum modularity (Figure 4). The position of these nodes at the top of the

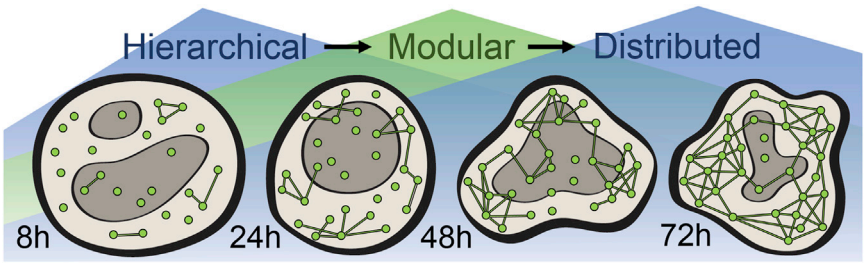

Figure 7. Proposed model for nervous system reassembly

As *Hydra* cellular aggregates regenerate, patterns of neural activity indicate an early peak in the hierarchical structure of the network as proto-circuits begin to form. Network activity then progresses through an intermediate state of high modularity, beginning with a containment hierarchy at 24 h as proto-circuits begin to synchronize into the larger modules observed at 48 h. Modularity at 24 and 48 h is characterized by loss of hierarchical depth during the transition to a distributed system. At 48 h, intermodule interaction of submodules appears, leading to synchronization across the entire animal at 72 h in a distributed network structure.

hierarchy places them in a unique position for "pattern completion" between the proto-modules or the *Hydra* equivalent. The data support a model where pattern completion may arise at this near decomposability of circuits into their subordinate functions and information representations and also suggest a flexibility for this feature, depending on circuit stability, given that, as *Hydra*'s circuits mature, this feature is lost. The flexibility of processing in the mammalian cortex potentially leaves this feature open, creating an inherent hierarchy at the overlap of this functional decomposition.

This initial work characterizing the *de novo* reassembly of a nervous system could lead to additional experimental and theoretic efforts toward understanding biological self-organization and the functional development of neural circuitry, particularly with respect to neuronal ensembles as natural functional modules present from cnidarians to mammals. Future studies using improved transgenic animals, tracking protocols, and optogenetic methods may allow further interrogation of *Hydra*'s developing neural circuitry and its emergent function. Our results demonstrate a change in the influence of individual neurons as circuits stabilize with development, a finding that may have implications beyond development for more complex nervous systems.

STAR★METHODS

Detailed methods are provided in the online version of this paper and include the following:

- KEY RESOURCES TABLE
- RESOURCE AVAILABILITY
  - Lead contact
  - Materials availability
  - Data and code availability
- EXPERIMENTAL MODEL AND SUBJECT DETAILS
  - Hydra
- METHOD DETAILS
  - Hydra dissociation/reaggregation
  - Imaging
- QUANTIFICATION AND STATISTICAL ANALYSIS
  - Image pre-processing
  - Cell tracking and neuron identification
  - Manual annotation of animal-wide activity
  - Spike extraction
  - Data analysis
  - Statistics

SUPPLEMENTAL INFORMATION

Supplemental information can be found online at https://doi.org/10.1016/j.cub.2021.06.047.

A video abstract is available at https://doi.org/10.1016/j.cub.2021.06.047#mmc8.

ACKNOWLEDGMENTS

We thank C. Dupre for transgenic lines and T. Lagache for cell tracking software and codes, other members of the Yuste Lab and the MBL *Hydra* Lab for assistance, and A. Fairhall and R. Steele for discussions. This material is based upon work supported by the Defense Advanced Research Projects Agency (DARPA) under contract no. HR0011-17C-0026, the NSF (CRCNS 1822550), and the Vannevar Bush Faculty Award (ONR N000142012828). J.R.L. was supported by the NIH (5 T32 GM 8798-18). R.Y. was a recipient of a Burroughs Wellcome Fund 2018 Collaborative Research Travel Grant. The *Hydra* Lab at the Marine Biological Laboratory (MBL) was supported in part by competitive fellowship funds from the H. Keffer Hartline; Edward F. MacNichol, Jr. Fellowship Fund; the E. E. Just Endowed Research Fellowship Fund; the Lucy B. Lemann Fellowship Fund; the Frank R. Lillie Fellowship Fund; the Fries Trust Research Award; the Hartline MacNichol Research Award; the L. & A. Colvin Summer Research Fellowship; and the John M. Arnold Fellowship Research Award.

AUTHOR CONTRIBUTIONS

J.R.L. and R.Y. conceptualized the work and designed experiments. J.R.L. conducted experiments and analysis. J.R.L. wrote the initial manuscript. J.R.L. and R.Y. edited the paper. R.Y. directed the project and secured funding.

DECLARATION OF INTERESTS

The authors declare no competing interests.

Received: February 16, 2021
Revised: May 14, 2021
Accepted: June 16, 2021
Published: July 22, 2021

REFERENCES

1. Lorenz, D.M., Jeng, A., and Deem, M.W. (2011). The emergence of modularity in biological systems. Phys. Life Rev. *8*, 129–160.
2. Sporns, O., and Betzel, R.F. (2016). Modular brain networks. Annu. Rev. Psychol. *67*, 613–640.
3. Simon, H.A. (1962). The Architecture of Complexity (Springer), pp. 457–476.
4. Dupre, C., and Yuste, R. (2017). Non-overlapping neural networks in Hydra vulgaris. Curr. Biol. *27*, 1085–1097.

5. Bosch, T.C.G., Klimovich, A., Domazet-Lošo, T., Gründer, S., Holstein, T.W., Jékely, G., Miller, D.J., Murillo-Rincon, A.P., Rentzsch, F., Richards, G.S., et al. (2017). Back to the basics: cnidarians start to fire. Trends Neurosci. *40*, 92–105.
6. Gierer, A., Berking, S., Bode, H., David, C.N., Flick, K., Hansmann, G., Schaller, H., and Trenkner, E. (1972). Regeneration of Hydra from reaggregated cells. Nat. New Biol. *239*, 98–101.
7. Agata, K., Saito, Y., and Nakajima, E. (2007). Unifying principles of regeneration I: Epimorphosis versus morphallaxis. Dev. Growth Differ. *49*, 73–78.
8. Szymanski, J.R., and Yuste, R. (2019). Mapping the whole-body muscle activity of Hydra vulgaris. Curr. Biol. *29*, 1807–1817.e3.
9. Lagache, T., Hanson, A., Fairhall, A., and Yuste, R. (2020). Robust Single Neuron Tracking of Calcium Imaging in Behaving Hydra (Cold Spring Harbor Laboratory).
10. Lagache, T., Lansdell, B., Tang, J., Yuste, R., and Fairhall, A.L. (2018). Tracking activity in a deformable nervous system with motion correction and point-set registration. bioRxiv. https://doi.org/10.1101/373035.
11. Siebert, S., Farrell, J.A., Cazet, J.F., Abeykoon, Y., Primack, A.S., Schnitzler, C.E., and Juliano, C.E. (2019). Stem cell differentiation trajectories in *Hydra* resolved at single-cell resolution. Science *365*, eaav9314.
12. Noro, Y., Shimizu, H., Mineta, K., and Gojobori, T. (2020). A Single Neuron Subset Governs a Single Coactive Neuron Circuit in Hydra vulgaris, Representing a Prototypic Feature of Neural Evolution (Cold Spring Harbor Laboratory).
13. Seybold, A., Salvenmoser, W., and Hobmayer, B. (2016). Sequential development of apical-basal and planar polarities in aggregating epithelio-muscular cells of Hydra. Dev. Biol. *412*, 148–159.
14. Bosch, T.C. (2007). Why polyps regenerate and we don't: towards a cellular and molecular framework for Hydra regeneration. Dev. Biol. *303*, 421–433.
15. Kirkby, L.A., Sack, G.S., Firl, A., and Feller, M.B. (2013). A role for correlated spontaneous activity in the assembly of neural circuits. Neuron *80*, 1129–1144.
16. Richter, L.M., and Gjorgjieva, J. (2017). Understanding neural circuit development through theory and models. Curr. Opin. Neurobiol. *46*, 39–47.
17. Warp, E., Agarwal, G., Wyart, C., Friedmann, D., Oldfield, C.S., Conner, A., Del Bene, F., Arrenberg, A.B., Baier, H., and Isacoff, E.Y. (2012). Emergence of patterned activity in the developing zebrafish spinal cord. Curr. Biol. *22*, 93–102.
18. Wan, Y., Wei, Z., Looger, L.L., Koyama, M., Druckmann, S., and Keller, P.J. (2019). Single-cell reconstruction of emerging population activity in an entire developing circuit. Cell *179*, 355–372.e23.
19. Rubinov, M., and Sporns, O. (2010). Complex network measures of brain connectivity: uses and interpretations. Neuroimage *52*, 1059–1069.
20. Bak, P., Tang, C., and Wiesenfeld, K. (1987). Self-organized criticality: an explanation of the 1/f noise. Phys. Rev. Lett. *59*, 381–384.
21. Clauset, A., Shalizi, C.R., and Newman, M.E.J. (2009). Power-law distributions in empirical data. SIAM Rev. *51*, 661–703.
22. Ravasz, E., and Barabási, A.L. (2003). Hierarchical organization in complex networks. Phys. Rev. E Stat. Nonlin. Soft Matter Phys. *67*, 026112.
23. Guimerà, R., Mossa, S., Turtschi, A., and Amaral, L.A.N. (2005). The worldwide air transportation network: anomalous centrality, community structure, and cities' global roles. Proc. Natl. Acad. Sci. USA *102*, 7794–7799.
24. Li, Y., Li, W., Tan, Y., Liu, F., Cao, Y., and Lee, K.Y. (2017). Hierarchical decomposition for betweenness centrality measure of complex networks. Sci. Rep. *7*, 46491.
25. Ten Tusscher, K.H., and Hogeweg, P. (2011). Evolution of networks for body plan patterning; interplay of modularity, robustness and evolvability. PLoS Comput. Biol. *7*, e1002208.
26. Wagner, G.P., and Altenberg, L. (1996). Perspective: complex adaptations and the evolution of evolvability. Evolution *50*, 967–976.
27. Espinosa-Soto, C., and Wagner, A. (2010). Specialization can drive the evolution of modularity. PLoS Comput. Biol. *6*, e1000719.
28. Carrillo-Reid, L., Han, S., Yang, W., Akrouh, A., and Yuste, R. (2019). Controlling visually guided behavior by holographic recalling of cortical ensembles. Cell *178*, 447–457.e5.
29. Ronhovde, P., and Nussinov, Z. (2010). Local resolution-limit-free Potts model for community detection. Phys. Rev. E Stat. Nonlin. Soft Matter Phys. *81*, 046114.
30. Blondel, V.D., Guillaume, J.-L., Lambiotte, R., and Lefebvre, E. (2008). Fast unfolding of communities in large networks. J. Stat. Mech. *2008*, P10008.
31. Lancichinetti, A., and Fortunato, S. (2012). Consensus clustering in complex networks. Sci. Rep. *2*, 336.
32. Jeub, L.G.S., Sporns, O., and Fortunato, S. (2018). Multiresolution consensus clustering in networks. Sci. Rep. *8*, 3259.
33. Traag, V.A., Krings, G., and Van Dooren, P. (2013). Significant scales in community structure. Sci. Rep. *3*, 2930.
34. Fortunato, S., and Barthélemy, M. (2007). Resolution limit in community detection. Proc. Natl. Acad. Sci. USA *104*, 36–41.
35. Bassett, D.S., and Sporns, O. (2017). Network neuroscience. Nat. Neurosci. *20*, 353–364.
36. Betzel, R.F., and Bassett, D.S. (2017). Multi-scale brain networks. Neuroimage *160*, 73–83.
37. Han, J., Li, W., and Deng, W. (2016). Multi-resolution community detection in massive networks. Sci. Rep. *6*, 38998.
38. Gireesh, E.D., and Plenz, D. (2008). Neuronal avalanches organize as nested theta- and beta/gamma-oscillations during development of cortical layer 2/3. Proc. Natl. Acad. Sci. USA *105*, 7576–7581.
39. Butts, D.A., Feller, M.B., Shatz, C.J., and Rokhsar, D.S. (1999). Retinal waves are governed by collective network properties. J. Neurosci. *19*, 3580–3593.
40. Beggs, J.M., and Plenz, D. (2004). Neuronal avalanches are diverse and precise activity patterns that are stable for many hours in cortical slice cultures. J. Neurosci. *24*, 5216–5229.
41. Beggs, J.M., and Plenz, D. (2003). Neuronal avalanches in neocortical circuits. J. Neurosci. *23*, 11167–11177.
42. Karimipanah, Y., Ma, Z., Miller, J.K., Yuste, R., and Wessel, R. (2017). Neocortical activity is stimulus- and scale-invariant. PLoS ONE *12*, e0177396.
43. Rubinov, M., Sporns, O., Thivierge, J.P., and Breakspear, M. (2011). Neurobiologically realistic determinants of self-organized criticality in networks of spiking neurons. PLoS Comput. Biol. *7*, e1002038.
44. Pallasdies, F., Goedeke, S., Braun, W., and Memmesheimer, R.M. (2019). From single neurons to behavior in the jellyfish *Aurelia aurita*. eLife *8*, e50084.
45. Kaiser, M., Görner, M., and Hilgetag, C.C. (2007). Criticality of spreading dynamics in hierarchical cluster networks without inhibition. New J. Phys. *9*, 110.
46. Kashtan, N., and Alon, U. (2005). Spontaneous evolution of modularity and network motifs. Proc. Natl. Acad. Sci. USA *102*, 13773–13778.
47. Kashtan, N., Noor, E., and Alon, U. (2007). Varying environments can speed up evolution. Proc. Natl. Acad. Sci. USA *104*, 13711–13716.
48. Clune, J., Mouret, J.B., and Lipson, H. (2013). The evolutionary origins of modularity. Proc. Biol. Sci. *280*, 20122863.
49. Mengistu, H., Huizinga, J., Mouret, J.B., and Clune, J. (2016). The evolutionary origins of hierarchy. PLoS Comput. Biol. *12*, e1004829.
50. Rieu, J.P., Upadhyaya, A., Glazier, J.A., Ouchi, N.B., and Sawada, Y. (2000). Diffusion and deformations of single hydra cells in cellular aggregates. Biophys. J. *79*, 1903–1914.
51. Yamamoto, W., and Yuste, R. (2020). Whole-body imaging of neural and muscle activity during behavior in Hydra vulgaris: effect of osmolarity on contraction bursts. eNeuro *7*, ENEURO.0539-19.2020.
52. Thummler, J. (2014). Nerve Cell Morphology and Neuronal Connectivity in Hydra (Ludwig-Maximilians-Universitat), p. 57.

53. Han, S., Taralova, E., Dupre, C., and Yuste, R. (2018). Comprehensive machine learning analysis of *Hydra* behavior reveals a stable basal behavioral repertoire. eLife *7*, e32605.

54. Tzouanas, C.N., Kim, S., Badhiwala, K.N., Avants, B.W., and Robinson, J.T. (2019). Thermal Stimulation Temperature Is Encoded as a Firing Rate in a Hydra Nerve Ring (Cold Spring Harbor Laboratory).

55. Wang, S.J., Hilgetag, C.C., and Zhou, C. (2011). Sustained activity in hierarchical modular neural networks: self-organized criticality and oscillations. Front. Comput. Neurosci. *5*, 30.

56. Wang, S.-J., and Zhou, C. (2012). Hierarchical modular structure enhances the robustness of self-organized criticality in neural networks. New J. Phys. *14*, 023005.

57. Russo, R., Herrmann, H.J., and de Arcangelis, L. (2014). Brain modularity controls the critical behavior of spontaneous activity. Sci. Rep. *4*, 4312.

58. Ponce-Alvarez, A., Jouary, A., Privat, M., Deco, G., and Sumbre, G. (2018). Whole-brain neuronal activity displays crackling noise dynamics. Neuron *100*, 1446–1459.e6.

59. Lenhoff, H.M., and Brown, R.D. (1970). Mass culture of hydra: an improved method and its application to other aquatic invertebrates. Lab. Anim. *4*, 139–154.

60. Wittlieb, J., Khalturin, K., Lohmann, J.U., Anton-Erxleben, F., and Bosch, T.C.G. (2006). Transgenic Hydra allow in vivo tracking of individual stem cells during morphogenesis. Proc. Natl. Acad. Sci. USA *103*, 6208–6211.

61. Edelstein, A., Amodaj, N., Hoover, K., Vale, R., and Stuurman, N. (2010). Computer control of microscopes using μManager. Curr. Protoc. Mol. Biol. *Chapter 14*, 20.

62. Lagache, T., Nardi, G., Bertot, L., Grassart, A., Sauvonnet, N., and Olivo-Marin, J. (2017). Combining global tracking with statistical classification to analyze endocytosis dynamics using TIRF microscopy. IEEE 14th International Symposium on Biomedical Imaging (ISBI 2017) (IEEE), pp. 1092–1095.

63. Ulman, V., Maška, M., Magnusson, K.E.G., Ronneberger, O., Haubold, C., Harder, N., Matula, P., Matula, P., Svoboda, D., Radojevic, M., et al. (2017). An objective comparison of cell-tracking algorithms. Nat. Methods *14*, 1141–1152.

64. Lancichinetti, A., and Fortunato, S. (2009). Community detection algorithms: a comparative analysis. Phys. Rev. E Stat. Nonlin. Soft Matter Phys. *80*, 056117.

65. Reichardt, J., and Bornholdt, S. (2006). Statistical mechanics of community detection. Phys. Rev. E Stat. Nonlin. Soft Matter Phys. *74*, 016110.

66. Reichardt, J., and Bornholdt, S. (2006). When are networks truly modular? Physica D *224*, 20–26.

67. Norton, H.K., Emerson, D.J., Huang, H., Kim, J., Titus, K.R., Gu, S., Bassett, D.S., and Phillips-Cremins, J.E. (2018). Detecting hierarchical genome folding with network modularity. Nat. Methods *15*, 119–122.

68. Shmiel, T., Drori, R., Shmiel, O., Ben-Shaul, Y., Nadasdy, Z., Shemesh, M., Teicher, M., and Abeles, M. (2005). Neurons of the cerebral cortex exhibit precise interspike timing in correspondence to behavior. Proc. Natl. Acad. Sci. USA *102*, 18655–18657.

STAR★METHODS

KEY RESOURCES TABLE

REAGENT or RESOURCE	SOURCE	IDENTIFIER
Experimental models: organisms/strains		
Hydra vulgaris strain AEP	Dr. Robert Steele, UC Irvine	N/A
Recombinant DNA		
pHyVec1	Addgene	RRID: Addgene_34789
GCaMP6s Synthetic Gene	GeneArt	Custom

RESOURCE AVAILABILITY

Lead contact

Further information and requests for resources and reagents should be directed to and will be fulfilled by the Lead Contact, Jonathan Lovas (jl4548@columbia.edu).

Materials availability

This study did not generate new unique reagents.

Data and code availability

The data and codes generated or analyzed during this study are available through Dryad. Ensemble synchronization in the reassembly of Hydra's nervous system, Dryad, Dataset, https://doi.org/10.5061/dryad.k6djh9w6k. All data are archived at the NeuroTechnology Center at Columbia University.

EXPERIMENTAL MODEL AND SUBJECT DETAILS

Hydra

Hydra vulgaris (Strain AEP) expressing GCaMP6s in the interstitial stem cell lineage under control of an actin promoter were cultured in the dark at 18°C in standard media as previously described.[4,59,60] Freshly hatched *Artemia* nauplii were fed to the animals every other day.

METHOD DETAILS

Hydra dissociation/reaggregation

For experiments, the dissociation and reaggregation of *Hydra* were performed as previously described[6] with minor modifications. In brief, after 48hrs starvation, 40-50 medium-sized *Hydra* were collected in a 3.5cm dish, washed thoroughly with room-temperature *Hydra* medium (RTHM) five times, washed quickly with ice-cold deionized water five times, and resuspended in ice-cold Gierer dissociation media (DM) - prepared from frozen concentrate - in a 1.5mL tube with one DM exchange. *Hydra* were incubated at 4°C for 2 hours, with media exchanges every ½ hour after vigorous resuspension of the animals with an unpolished Pasteur pipette. After 2 hours, DM was exchanged again and *Hydra* were triturated until the media became cloudy, indicating the start of tissue dissociation. After this, DM was exchanged one last time, and *Hydra* were mechanically dissociated with a new unpolished Pasteur pipette firmly at a constant rate avoiding bubbles ~75-125 times until approximately one-half to one third of the volume of intact tissue remained. Tissue fragments were allowed to sediment 90 s and the top $^{3}/_{4}$ of the cell suspension was gently collected.

Cells were counted on a hemocytometer and seeded in 0.5mL microcentrifuge tubes in numbers according to the requirements of the experiment, in this case 9k cells. We note that while most cells were single in suspension, a small percentage of cells (< 10%) remained in tiny aggregates of ~2-10 cells. Due to their small size, filtration through standard filters was unable to break these aggregates, assuming the cells were not aggregating after complete dissociation in the time before cell counting. Cells were allowed to sediment on ice for 5 minutes, then centrifuged at 4°C for 4 minutes at 300 g in an Eppendorf 5430 R centrifuge. From here, pellets in 0.5mL microcentrifuge tubes were placed at 18°C and incubated for 2 hours, 3cm above a bed of melting ice to slow the temperature transition. Pellets were transferred to 800μL dissociation media after two hours. At 8 hours after dissociation, media was diluted 50% with 800μL *Hydra* media at 18°C, and again with a 50% HM replacement at 22 hours, 46 hours, and 70 hours. *Hydra* in all experiments survived the dissociation procedure and developed into normal *Hydra*.

Imaging

Hydra were imaged as previously described,[4] using 100 μm spacers between coverslips for the imaging sessions. Analyzed images were acquired on an Olympus IX70 inverted fluorescence microscope equipped with a GFP filter set, 10x Plan Apo air objective, and a

Hamamatsu C9913-EMCCD camera using Micromanager.[61] This setup was illuminated by a mercury arc lamp. Images were acquired at 100% illumination intensity, at 250ms exposure, 1x binning, for 7200 frames (~42.1 minutes with CCD charge transfer time). Intact animals were imaged on a Leica M165 FC fluorescence dissection microscope as previously described.[4]

QUANTIFICATION AND STATISTICAL ANALYSIS

Image pre-processing

Images were pre-processed in FiJi. For tracking, either 2 (Intact Animals; 48, 72 hour aggregates) or 10 (Dissociated Cells; 8, 24 hour aggregates) frames were summed, background was subtracted with a 10 pixel rolling ball radius, and a 3-pixel diameter median filter was applied. After tracking, all 7200 frames of each experiment were similarly background subtracted and median filtered for extraction of continuous track fluorescence, interpolating (x,y) positions across 10 or 2 frames, depending on the time point.

Cell tracking and neuron identification

Cells were tracked using the open-source cell tracking software ICY,[10,62] using parameters tuned to the unique requirements of experiments across time points (Data S1A). Spatial coordinates of each track were imported into MATLAB and used to extract fluorescence intensity from pre-processed images with the maximum values along each axis of a 7x7 pixel square around the detected track. The deformable hydrostatic skeleton of *Hydra* makes tracking cells over large movements difficult. While this problem is remedied to some extent in reaggregating *Hydra*, especially at early time points when there is not much movement, inaccuracies in cell tracking still exist (Figure S1; Data S1G). Even under static conditions of fluorescence, cell tracking is an unresolved problem and manual curation is necessary to approach flawless results.[63] To ensure accuracy in tracking across experiments, misaligned or broken tracks were manually corrected, and inaccuracies in neuron identification (e.g., autofluorescent spots passing under tissue) were excluded (Video S1; Data S1G).

The final analysis was conducted on frames 571-5700 of the original 7200 frames acquired at 2.85*hz* for several reasons. The dropped time at the start of the experiments allowed the animals to equilibrate to the intense illumination. In addition, this period of time offset some of the effects of photobleaching, as autofluorescent spots on the aggregate bleached rapidly with intense illumination, and GCaMP began to dim toward the end of the imaging session (Figure S1A). Finally, the tracking software ICY did not handle the ends of some tracks well, and cutting time removed some bouts of track activity that weren't picked up at either end of the experiment.

Manual annotation of animal-wide activity

The two main forms of neural activity in *Hydra* – contraction bursts and rhythmic potentials – were manually annotated in 72 hour aggregates and intact animals for analysis. We began analysis on the first contraction burst that followed a period of quiescence and ended analysis on the last complete contraction burst followed by a period of quiescence within the 30 minute period of analysis. Given that a subset of contraction burst neurons sometimes fires before the remaining CB neurons are recruited to the burst, we began our annotation of pulses of contraction burst activity with the first firing of the dominant, early subset of neurons in the burst. We note that the analysis of rhythmic potentials was conducted on the Rhythmic Potential 1 circuitry, as the activity of Rhythmic Potential 2 was very rare, if present at all, in the 30 minute imaging sessions.[4]

Spike extraction

To account for the effects of mild photobleaching on fluorescence intensity traces, aggregates were segmented in MATLAB and changes in the overall fluorescence intensity across the entire segmented aggregate were subtracted from fluorescence intensity traces using an X-frame sliding window (Figure S2), after smoothing raw fluorescence traces with a 2nd-degree polynomial Savitzky-Golay filter. From here, MATLAB's 'findpeaks' algorithm was used to detect both the maximum of the filtered fluorescence intensity as well as the maximum and minima of the local first derivative of fluorescence intensity of the peaks, using a threshold of standard deviation and wider sliding averages exclude peaks in the signal generated by noise or broad sub-spike-threshold calcium fluctuations. 'Spikes' were defined around the maximum and minimum of the first derivative of fluorescence intensity to account for differences in spiking kinetics of different classes of neurons (Figures S1 and S2; Data S1H). From here, two additional thresholds were applied to compensate for the effects of photobleaching on the intensity of tracks throughout the experiment, and to exclude noisy autofluorescent spots from analysis. The final analysis was conducted on tracks that were active at least 1/3 of the 30 minute experiment, firing at a frequency of at least 1/180/p(active)*hz* (10 spikes).

Data analysis

Spike rasters were used to generate adjacency matrices for analysis. To account for the differences in the duration of spiking events of individual neurons at the imaging framerate, correlations between neurons were based on the normalized coactivity (a final value between zero and one, if they never or always fired together, respectively). Studies of functional connectivity did not take the distance between neurons into account. Studies of neuron distribution within communities and waves of neuronal activity that permeate the system took into account the fact that Hydra's neuron's limited number of neurites don't project long distances in most cases (Figure 1; Data S1G).[4,52] To provide a rough proxy for structural connectivity in analysis of propagation of activity through the network, we used conservative estimates: the average length of the longest neurite per neuron of 48 hour aggregates (62 μm; Figures S1 and S5),

the average length of neurites multiplied by 2 to allow connections between distal neurites (115 μm; Figures 6 and S1), as well as a more liberal estimate: the average length of the longest neurite per neuron, multiplied by 3, to account for any potential incomplete labeling in neurons of aggregates or dim distal extremities of neurites (185 μm; Figures S1 and S6).

To determine 'significant functional connections' for edges in metrics calling for unweighted, undirected networks, for each pair of nodes in the network we circularly shifted the spike trains at uniformly distributed random intervals 1000 times to reveal a probability distribution for the observed coactivity between the neurons. To avoid error propagation within a fairly liberal null model thresholded at a standard a standard $\alpha = 0.05$, we used the most stringent threshold that would allow analysis of our chosen network properties to limit the chance addition of spuriously significant edges to the network (e.g., significant network $\alpha = 0.005$ versus $\alpha = 0.05$, Figures 3 and S3A; Data S1C and S1I). We note that significant coactivity is presumably mediated by chains of physical connections/synapses if this distance was longer than twice our observed neurite lengths.

As controls to understand effects of network size and connection density, we compared our network metrics to binary networks randomized by circularly shifting adjacency matrices along both axes 20 times to generate p = 0.05 density-preserving null distributions for our metrics (Figures 4A, 4B, 4D, and 4E, dashed lines; Data S1D). As a control for the inevitable removal of nodes from the developing network, we also analyzed our models with random subsets of 20% of the nodes removed, approximately the number lost at each successive time point (18.21+/−5.8%; Figure S3B, dashed lines; Data S1I).

To uncover community structure in our network models, we use the Louvain method of modularity maximization. This greedy method is fast and precise, and performs better than other methods when presented with network modules comprised of different numbers of nodes.[64] In addition to other graph theoretic analysis in the present work, Louvain consensus community clustering makes use of the Brain Connectivity Toolbox.[19] In brief, the method heuristically optimizes modularity, a measure of the density of edges inside communities to edges outside communities, by first optimizing modularity locally on all nodes, then grouping these small communities into a node and reiterating.[30] The Louvain method is particularly appropriate for studies of hierarchical modularity, as the iterative method inherently reflects any containment hierarchy in the network structure. To reconcile variability in detected communities due to the random initiation of nodes at the start of each iteration of the algorithm, we use the final consensus communities after 1000 runs of the algorithm, clustering the final consensus matrix of agreement values reflecting similar partitioning between nodes with $\tau = 0$ to ensure as many nodes as possible were clustered (Figure S4A; Data S1J).[31]

With consensus communities in place, to ensure optimal partitioning with the method we then varied the resolution parameter γ, a modification to the modularity objective function which increasingly penalizes out-of-community connections to tune the density of detected communities.[32–34,65,66] In essence, higher gamma values favor detection of smaller, more densely intraconnected communities. Given the stochastic initiation of the algorithm, to ensure we were looking at a stable partition of the weighted network we used the 'plateau method', sweeping the resolution parameter γ of the modularity objective function Q from 0.6 to 3 (e.g., Figure S4B and Data S1J), using communities from the plateau of identical partitions across at least 3 increasing γ increments of 0.01 that gave the largest value of Q.[34,67] Sub-partitioning of the modules of this initial partition was performed with $\gamma = 1$. Analysis of trends in the values γ sweep in Figures S4B and S4C was performed with plateaus of length > = 0.02 γ increments to provide more data points for analysis.

Waves of activity, or 'neuronal avalanches,' depending on the field, were determined using the metrics of structural connectivity defined above (Data S1G). Power-law plots where created using the MATLAB 'plplot' function.[21] Waves of activity were superimposed on Louvain communities using custom MATLAB code (supplemental material).

Statistics

We tested the significance of synchronization observed in our experiments against the null hypothesis that the synchronous firing of neurons is governed by a random process.[68] Randomized networks were used to establish confidence intervals to determine significant connectivity in analyses. Due to the variable length of spiking of *Hydra* neurons, random networks were created by randomly circularly shifting individual neuron tracks around the length of the experiment at uniformly distributed random locations, repeated 1000 times for each experiment.

For tests of the significance of network structure, the weights or binary values of the original adjacency matrix were randomized 20 times to generate p = 0.05 null distributions (Data S1D). The significance of data plotted in power law form was assessed using the non-parametric Wilcoxon Rank-Sum test of significance. Data presented in bar graphs was assessed using the non-parametric Mann-Whitney-Wilcoxon U-test. Bar graphs were generated using custom MATLAB code, and violin plots were generated using a modification of the 'violinplot' function in MATLAB (Bastian Bechtold, 2016).

Current Biology, Volume *31*

Supplemental Information

Ensemble synchronization in the reassembly of *Hydra*'s nervous system

Jonathan R. Lovas and Rafael Yuste

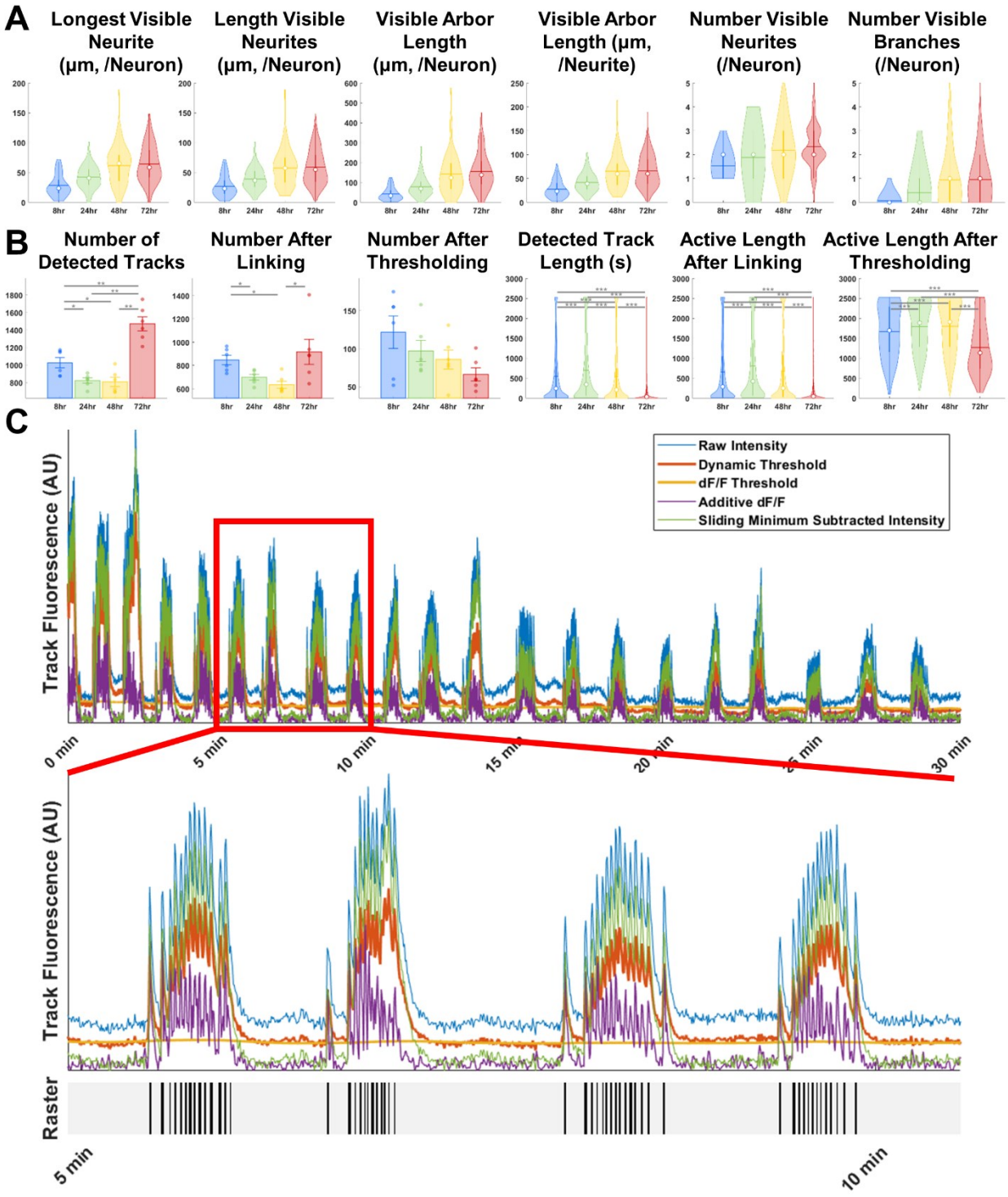

Figure S1. Neurites elongate during the first 48 hours of *Hydra* reaggregation and neuron tracking and GCaMP6s signal processing, Related to Figures 1, 6, S5, S6, STAR Methods, and Data S1G

A) Although previously characterized variability between neuron subtypes precludes statistically significant findings, trends exist toward an increase in the length of the longest visible neurite to 48 hours, the overall length of visible neurites to 48 hours, and the total visible arbor length per neuron and neurite to 48 hours. A trend toward an increase in the number of visible neurites and the number of visible branches per neuron and neurite exists to 48 hours**. B)** Significantly more tracks were detected at 8 hours and 72 hours, in part due to individual motility and sporadic activity of neurons at 8 hours and collective movement of the aggregate at 72 hours. After manually linking shorter tracks belonging to the same neuron, we observe fewer tracks in all cases, with the same trend of more tracks at 8 hours and 72 hours. After thresholding our tracks of interest to fluorescent points that spiked at a rate of 1/60hz for at least 10 minutes during the experiment, we observe a declining trend in the number of neurons per aggregate, consistent with the previously characterized cell loss that occurs during the process. Detected track length is significantly shorter at 8 and 72 hours for the same reason. Track length increases in all cases with the same trend. Active length increases after thresholding to remove autofluorescence. **C)** Traces of parameters used to threshold spikes from neurons, in this case a putative CB neuron at 48 hours (top, STAR Methods). Zooming in on the segment from 5 minutes to 10 minutes, the spike raster plot (bottom, detected spikes in black) corresponds well to the peaks of raw GCaMP6s fluorescence (light blue) obtained in experiments.

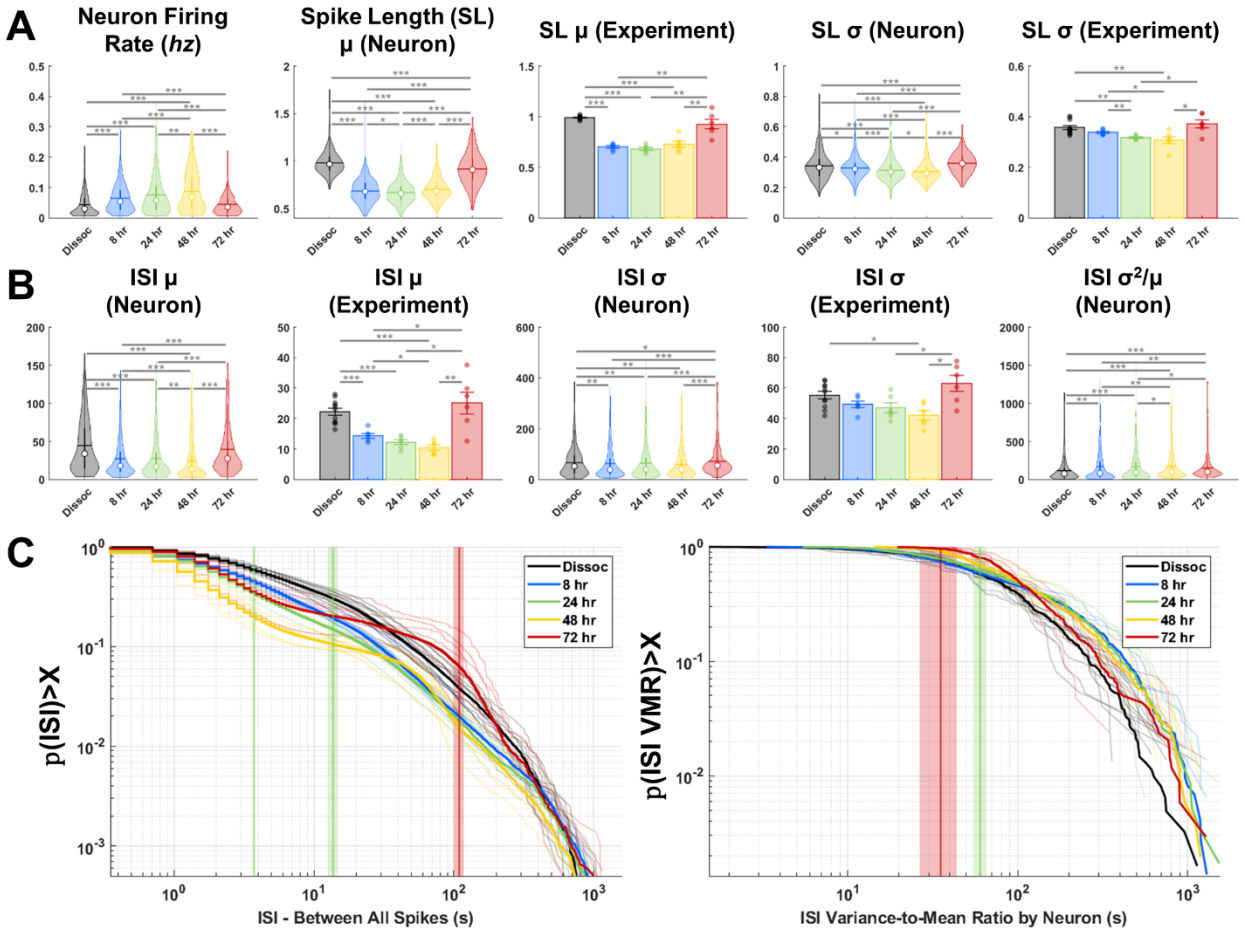

Figure S2. Detected spike statistics, Related to STAR Methods and Data S1H

Freshly dissociated cells were allowed to sediment in a 96-well glass bottom plate for thirty minutes, and were then imaged and analyzed similarly to aggregates. **A)** From left to right: We note significant increases in the firing rate of neurons to 48 hours, with a decline at 72 hours to frequencies similar to freshly dissociated cells. Spikes in neurons were generally longer at 72 hours and in freshly dissociated cells, consistent with residual calcium broadening spike peaks during animal-wide contraction bursts. Similar trends were observed for mean values by experiment, and the standard deviations of spike length by neuron and experiment, as would be expected with the stepwise increase in residual calcium during contraction bursts. **B)** From left to right: Conversely to neuron firing rate, spike inter-stimulus interval (ISI) was generally larger at 72 hours and in

freshly dissociated cells. The same trend holds true looking at experiment means. The ISI standard deviation was slightly higher in neurons of 72 hour aggregates and freshly dissociated neurons, and the trend was preserved for experiment means of the ISI standard deviations. The ISI variance to mean ratio was slightly lower at 72 hours and in dissociated cells. **C)** Descending cumulative distributions of all ISI values illustrate the reemergence of rhythmic patterns of activity (left). Vertical lines for the CB pulse ISI (green, left), CB overall ISI (green right), and RP ISI represent values obtained from analysis of animal-wide fluorescence (Figure 2). Note the from 8 hours to 48 hours as increasingly larger percentages of ISIs fall below the 'CB pulse' ISI vertical line, indicating the reestablishment of CB dynamics in absence of animal-wide synchronization. ISI variance-to-mean ratio by neuron indicates increasingly larger values to 72 hours until just after our values for whole animal CB ISI VMR (green vertical line), again consistent with the reestablishment of busting dynamics.

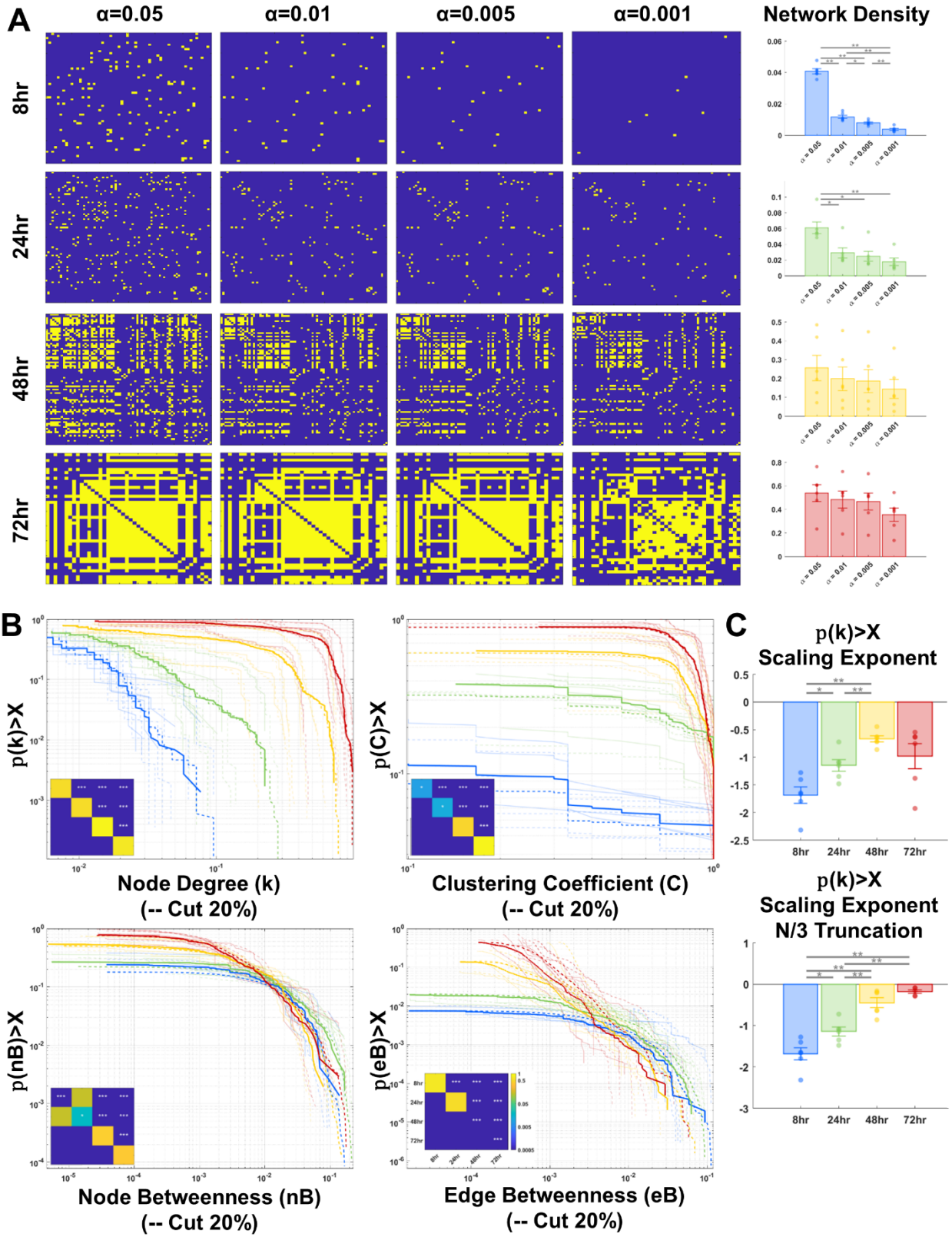
A
α=0.05
α=0.01
α=0.005
α=0.001
8hr
24hr
48hr
72hr
Network Density
B
p(k)>X
Node Degree (k)
(-- Cut 20%)
p(C)>X
Clustering Coefficient (C)
(-- Cut 20%)
p(nB)>X
Node Betweenness (nB)
(-- Cut 20%)
p(eB)>X
Edge Betweenness (eB)
(-- Cut 20%)
C
p(k)>X
Scaling Exponent
p(k)>X
Scaling Exponent
N/3 Truncation
8hr
24hr
48hr
72hr

Figure S3. Validation of network thresholding, network analysis with neuron loss, and scaling exponents for degree distribution power law fits, Related to Figures 3, 4, S4, and Data S1I

A) Adjacency matrices of networks of a representative experiment binarized at increasingly stringent thresholding alpha values, as determined by circularly shifting firing patterns between pairs of neurons at uniformly distributed random intervals 1000 times. Between pairs of neurons (along x and y axes) significant connections are depicted in yellow. Note the diminishing effect of increasing stringency at later time points. Binarized networks were ultimately analyzed at the α=0.005 time point to avoid error propagation within the fairly liberal standard threshold of α=0.05. **B)** To validate our network analysis given the previously characterized gradual loss of neurons from the regenerating animal, we removed 20% of nodes and their respective edges from the α=0.005 significant networks at random 20 times and conducted the same analysis on these randomly attacked networks. No significant differences exist in the degree distributions, comparing experimental values to the randomly truncated values along the diagonal of the significance matrix (top left). The clustering coefficient was generally lower in our randomly truncated networks at 8 hours and 24 hours, as would be expected in sparsely connected networks in which the clustering coefficient is more likely based on a single triangles (top right). A similar finding was observed for node betweenness (bottom left). Conversely, as edges are removed at later time points from denser graphs, these shortest paths must be redistributed, leading to an increase in betweenness centrality of the edges involved in redistribution. Note that in this case the probability of a node routing shortest-edge traffic remains unchanged (bottom right). **C)** The slope of the fit to give our scaling coefficient to characterize scale-free networks declines to 48 hours. If we consider that this metric saturates with the size of the circuits of our network, as is seen in the

shoulders of the distributions at 48 and 72 hours, fitting a distribution truncated to 1/3 the size of the network gives more accurate scaling coefficients across the first decade of the degree values.

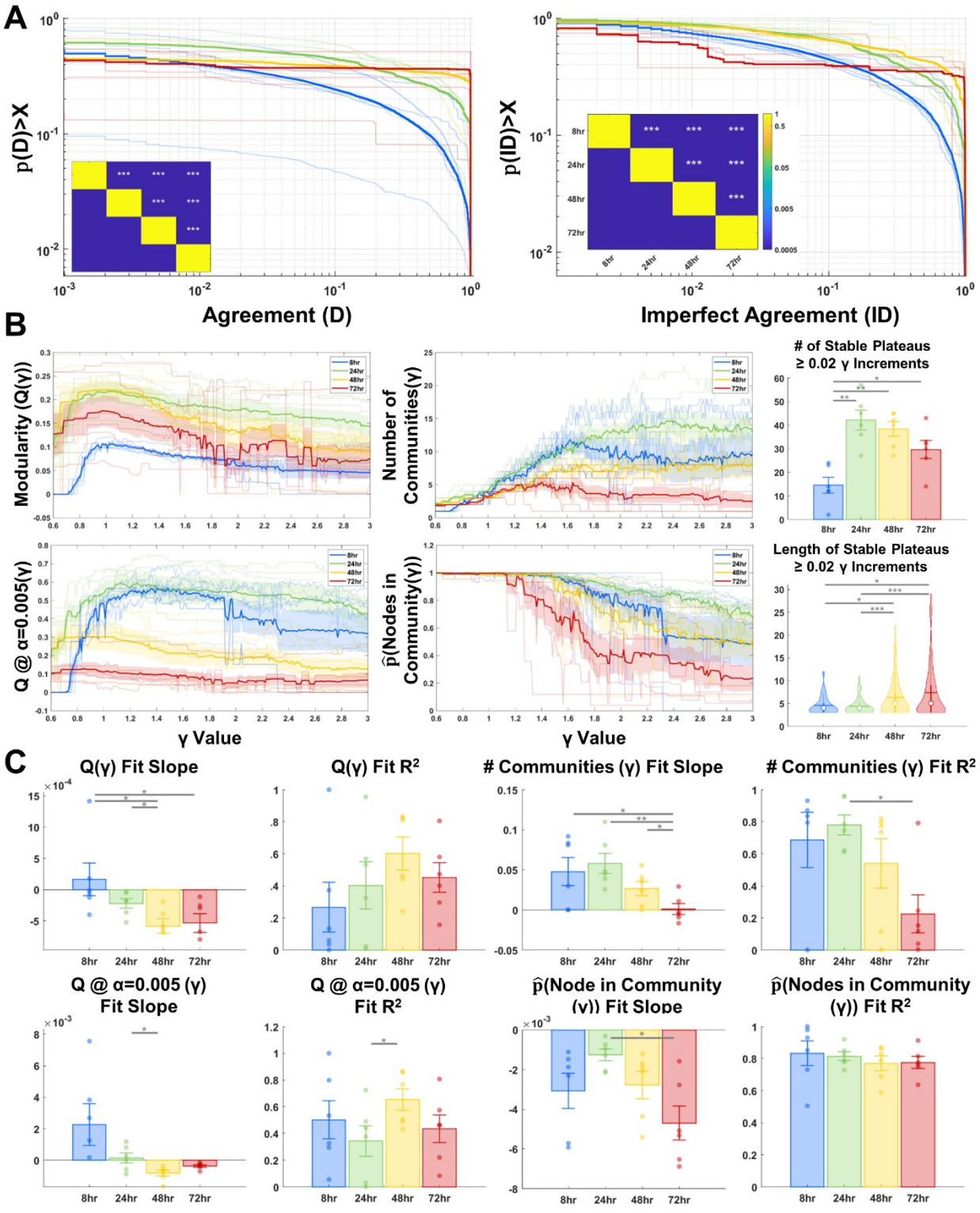

Figure S4. Consensus community clustering at maximum modularity and varied community detection gamma resolution, Related to Figures 5, 6, and Data S1J

Iterating the randomly-initialized Louvain community detection algorithm on a network 1000 times yields an agreement matrix with the number of times pairs of neurons were assigned the same community. We note gradual improvements in agreement, indicating increased stability of clustering until 48 hours – nodes are more likely to be grouped into the same community even with random initialization (left). Distributions of imperfect agreement, excluding values equal to zero or 1 (right). **B)** Modularity (top left), modularity of networks binarized at α=0.005 (bottom left), number of detected communities (top middle) and the proportion of nodes clustered into communities (bottom middle) as a function of varying the Louvain resolution parameter gamma from 0.6 to 3 in increments of 0.01. Given that the increases we observe in intra-/inter-community strength are largely driven by increasing intracommunity strength over time, the drastic increase in modularity and stability over our range of gamma values in networks binarized at the α=0.005 significance level is not surprising. We also observe an increase in the number of stable plateaus of at least 2 identical network partitions with increasing gamma values from 8 hours to 24 hours (top right) and a significant increase in the length of these stable plateaus from 24 to 48 hours (bottom right, extreme outliers >3xIQR not depicted). **C)** Slope and R^2 values of a first degree polynomial fit of the values in (B).

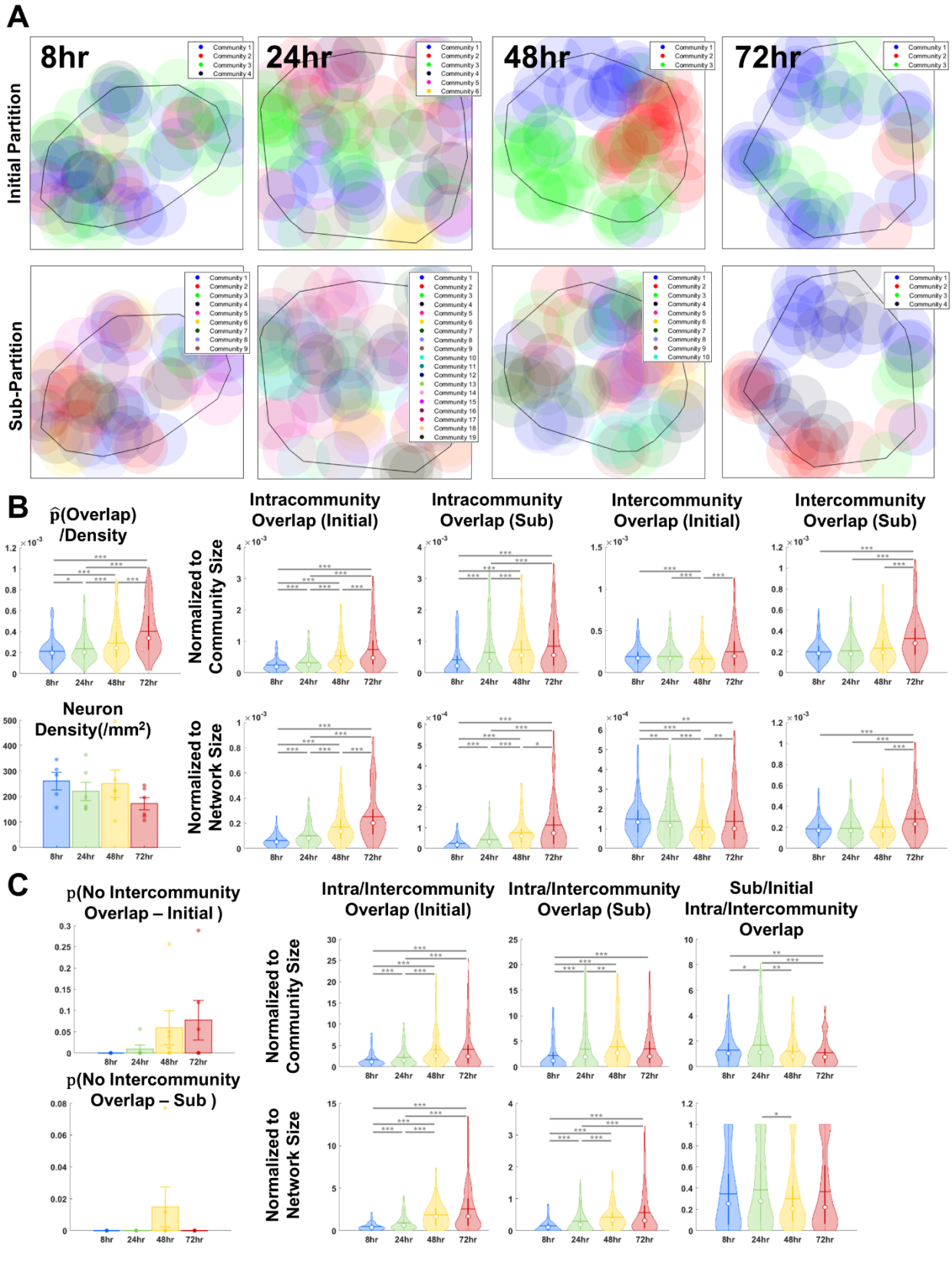
A
8hr
24hr
48hr
72hr
Initial Partition
Sub-Partition
B
p̂(Overlap) /Density
Intracommunity Overlap (Initial)
Intracommunity Overlap (Sub)
Intercommunity Overlap (Initial)
Intercommunity Overlap (Sub)
Neuron Density(/mm²)
Normalized to Community Size
Normalized to Network Size
C
p(No Intercommunity Overlap – Initial)
p(No Intercommunity Overlap – Sub)
Intra/Intercommunity Overlap (Initial)
Intra/Intercommunity Overlap (Sub)
Sub/Initial Intra/Intercommunity Overlap
Normalized to Community Size
Normalized to Network Size

Figure S5. Local interactions mediate the increases in modularity observed during reaggregation, Related to Figures 3, 5, and Data S1K

A) Representative spatial distribution of potential connections between neurons, using the average length of the longest neurite per neuron at 48 hours (61.83μm). Neurons are color coded by community based on the initial partition (top row) and sub-partition (bottom row). The outer boundary of the aggregate is depicted as the shortest path around the most peripheral neuron centers of the aggregate. **B)** Neurons are increasingly likely to overlap with others over time, and no significant differences in density are observed. Normalized to density, then either to the number of intra- or intercommunity nodes (top row), or network size (bottom row), we observe increases in the proportion of intracommunity overlap with time in both the initial and sub-partitions, as well as a decrease in intercommunity overlap at 48 hours for the initial partition, while 72 hour aggregates had the largest degree of intercommunity overlap for the sub-partition. **C)** Examining the ratios of intra- to intercommunity overlap, we first note small percentage of nodes with no intercommunity overlap which were excluded from analysis to avoid infinite values in the ratio, then gradual increases in this ratio to 48 hours in both the initial and sub-partitions. Importantly, as we move from the sub-partition to the initial partition in a 'ratio-of-ratios' we observe the largest increase at 24 hours, a reflection of the local optimization of protocircuits before their fusion into the larger, more spatially compact modules of the initial partition at 48 hours. Extreme outliers >3xIQR not depicted.

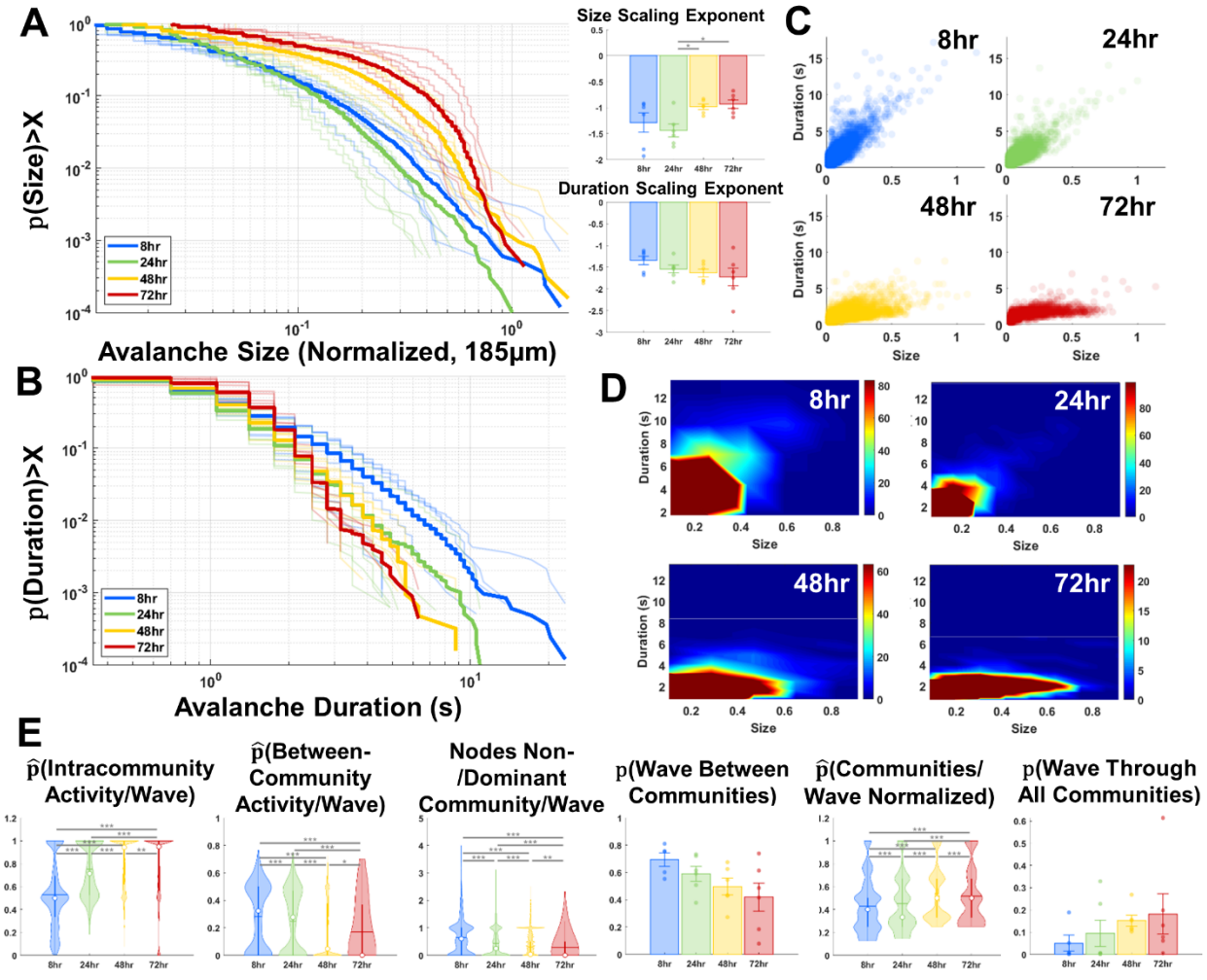

Figure S6. Avalanches recruit module sub-circuits during synchronization with a more liberal wave determination distance of 185µm, Related to Figure 6 and Data S1L

A) During the course of reaggregation, distributions of the sizes of neuronal avalanches (left) and critical exponents (top right) indicate a phase transition in activity of the regenerating nervous system as the system becomes increasingly supercritical. Note the clear shift in sizes along the x-axis is due to normalization to the number of nodes in the network, and that waves of activity were generated using a 185µm radius of coactivity (3 times the average neurite length of the longest neurite at 48 hours, Figure S1). **B)** Distributions of avalanche duration are not as distinct. **C)** Dots

plot of avalanche duration as a function of size. Note the distinct cluster at 48 hours. **D)** Heat maps providing more resolution of densely clustered points near the origin of the duration(size) plots. **E)** Superimposition of neuronal avalanches on detected Louvain communities at maximum modularity. From left to right: Coactivity of neurons within the avalanche wave radius of 115μm is increasingly likely to be in the same community to 48 hours. Coactivity between communities declines to 48 hours. Fewer nodes from a non-dominant community are likely to be recruited to a wave to 48 hours. Waves are increasingly less likely to spread between communities to 48 hours. A trend toward more communities per wave normalized to the total number of communities with time is present. A trend toward an increasing number of waves traveling through all communities is present.